Synthesis, Structure, and Spectroscopic and Magnetic Characterization of [Mn$_{12}$O$_{12}$(O$_2$CCH$_2$Bu^t)$_{16}$(MeOH)$_4$]·MeOH, a Mn$_{12}$ Single-Molecule Magnet with True Axial Symmetry

Christos Lampropoulos,[†,‖] Muralee Murugesu,[†,⊥] Andrew G. Harter,[‡] Wolfgang Wernsdofer,[#] Stephen Hill,[§] Naresh S. Dalal,[‡] Arneil P. Reyes,[§] Philip L. Kuhns,[§] Khalil A. Abboud,[†] and George Christou*,[†]

[†]Department of Chemistry, University of Florida, Gainesville, Florida 32611, United States
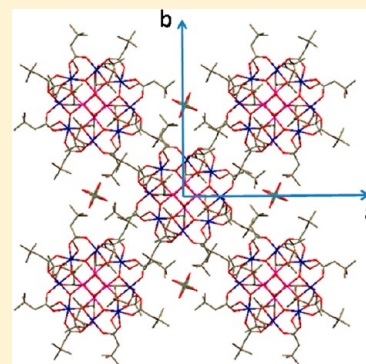
[‡]Department of Chemistry and Biochemistry, Florida State University, Tallahassee, Florida 32310, United States

[§]Department of Physics and National High Magnetic Field Laboratory, Florida State University, Tallahassee, Florida 32310, United States

[#]Institut Néel, CNRS/UJF, BP 166, 25 Avenue des Martyrs, 38042, Grenoble, Cedex 9, France

S *Supporting Information*

ABSTRACT: The synthesis and properties are reported of a rare example of a Mn$_{12}$ single-molecule magnet (SMM) in truly axial symmetry (tetragonal, $I\bar{4}$). [Mn$_{12}$O$_{12}$(O$_2$CCH$_2$Bu^t)$_{16}$(MeOH)$_4$]·MeOH (**3·MeOH**) was synthesized by carboxylate substitution on [Mn$_{12}$O$_{12}$(O$_2$CMe)$_{16}$(H$_2$O)$_4$]·2MeCO$_2$H·4H$_2$O (**1**). The complex was found to possess an $S = 10$ ground state, as is typical for the Mn$_{12}$ family, and displayed both frequency-dependent out-of-phase AC susceptibility signals and hysteresis loops in single-crystal magnetization vs DC field sweeps. The loops also exhibited quantum tunneling of magnetization steps at periodic field values. Single-crystal, high-frequency electron paramagnetic resonance spectra on **3·MeOH** using frequencies up to 360 GHz revealed perceptibly sharper signals than for **1**. Moreover, careful studies as a function of the magnetic field orientation did not reveal any satellite peaks, as observed for **1**, suggesting that the crystals of **3** are homogeneous and do not contain multiple Mn$_{12}$ environments. In the single-crystal ^{55}Mn NMR spectrum in zero applied field, three well-resolved peaks were observed, which yielded hyperfine and quadrupole splitting at three distinct sites. However, observation of a slight asymmetry in the Mn^{4+} peak was detectable, suggesting a possible decrease in the local symmetry of the Mn^{4+} site. Spin−lattice (T_1) relaxation studies were performed on single crystals of **3·MeOH** down to 400 mK in an effort to approach the quantum tunneling regime, and fitting of the data using multiple functions was employed. The present work and other recent studies continue to emphasize that the new generation of truly high-symmetry Mn$_{12}$ complexes are better models for thorough investigation of the physical properties of SMMs than their predecessors such as **1**.

INTRODUCTION

Single-molecule magnets (SMMs) are molecular nanoscale magnetic particles, and thus they provide a bottom-up, molecular approach to nanomagnetism.[1,2] SMMs are typically polynuclear assemblies of exchange-coupled paramagnetic metal ions, usually bridged by O-based ligands. Their molecular nature brings valuable advantages to the field of nanomagnetism, since molecular crystals provide three-dimensional (3-D) organizations of monodisperse particles of a well-defined size and (often) a single orientation. Their behavior as nanomagnets arises from their intramolecular properties of a large ground state spin (S) and Ising (easy-axis-type) anisotropy, reflected in a negative second-order axial zero-field splitting (ZFS) parameter (D), which leads to SMMs displaying magnetization hysteresis, the classical property of a magnet. SMMs have also served as exceptional models for studying complex quantum phenomena and exotic physical

properties such as quantum tunneling of the magnetization,[3] spin parity effects,[4,5a] quantum phase interference,[5] and magnetic deflagration,[6] among others.[7] As a result of this combination of classical and quantum properties, SMMs have been proposed as components in several advanced applications, including ultrahigh-density information storage, spintronics, and quantum computation.[8]

The [Mn$_{12}$O$_{12}$(O$_2$CR)$_{16}$(H$_2$O)$_4$] (R = various) family of SMMs is the most studied and best understood to date, having been the focus of numerous physical and spectroscopic studies for reasons that include the often high symmetry of these complexes, their reasonably well-isolated ground state spins, their ease of preparation from inexpensive materials, and their documented stability in the solid state and in solution, which

has also allowed their ready modification in a variety of ways.[9] The R = Me derivative, $[Mn_{12}O_{12}(O_2CMe)_{16}(H_2O)_4]\cdot 2MeCO_2H\cdot 4H_2O$ (**1**; Mn_{12}–Ac),[2a,10] has been very attractive for such reasons, being prepared in one step from simple reagents and crystallizing in tetragonal space group $I\bar{4}$. **1** is also an excellent starting point for synthesizing any other desired carboxylate derivative by employing the straightforward carboxylate substitution methodology we developed.[2a,9,11,12] This has allowed a variety of carboxylates to be introduced, including those with bulky R groups such as CMe_2Et, etc.[13] Mixed-carboxylate $[Mn_{12}O_{12}(O_2CR)_8(O_2CR')_8(H_2O)_4]$ species can also be prepared,[14] and partial substitution of carboxylates with anions of other organic and inorganic acids has also been achieved.[15] In addition, convenient methods have been reported allowing isolation and study of one-,[11a,16] two-[17] and three-electron[18] reduced species. Less well explored than carboxylate substitution is the preparation of $[Mn_{12}O_{12}(O_2CR)_{16}(R'OH)_4]$ derivatives containing terminal alcohol groups in place of the H_2O ligands. In most cases, the alcohol is MeOH,[13,19] but derivatives with the higher alcohols Bu^tOH and n-$C_5H_{11}OH$ have recently been reported.[20]

The realization that crystals of high-symmetry **1** in reality contain molecules spanning a range of local site-symmetries due to hydrogen-bonding contacts with n ($n = 0$–4) $MeCO_2H$ solvent molecules,[21] and that only the $n = 0$ and 4 species have the true S_4 site-symmetries of the $I\bar{4}$ space group, have stimulated a search for other derivatives crystallizing in high symmetry space groups but without local symmetry-lowering contacts with solvent molecules. A few such alternative Mn_{12} complexes have been identified: they typically have relatively small carboxylate R groups, such as the $[Mn_{12}O_{12}(O_2CMe)_{16}(MeOH)_4]$[19] and $[Mn_{12}O_{12}(O_2CCH_2Br)_{16}(H_2O)_4]\cdot 4CH_2Cl_2$[12,22] derivatives, but one has bulky R = CH_2Bu^t groups, $[Mn_{12}O_{12}(O_2CCH_2Bu^t)_{16}(MeOH)_4]\cdot MeOH$ (**3**);[23] the latter has also the additional advantage of better separated Mn_{12} molecules in the crystal. Such truly high symmetry Mn_{12} complexes have been found to be a source of superior data when studied by solid-state spectroscopic and micro-SQUID methods, compared to **1**.[7e,24] We herein report full details of the synthesis and characterization of complex **3** by crystallography, SQUID magnetometry, and high-frequency EPR (HFEPR) and solid-state ^{55}Mn NMR spectroscopies.

■ EXPERIMENTAL SECTION

Synthesis. All manipulations were performed under aerobic conditions using materials as received, except where otherwise noted. $[Mn_{12}O_{12}(O_2CMe)_{16}(H_2O)_4]\cdot 2MeCO_2H\cdot 4H_2O$ (**1**) was prepared as described elsewhere.[2a,10]

$[Mn_{12}O_{12}(O_2CCH_2Bu^t)_{16}(MeOH)_4]$ (3). Freshly prepared crystals of complex **1** (0.50 g, 0.24 mmol) were dissolved in MeOH (40 mL), and $Bu^tCH_2CO_2H$ (5 mL) was added under continuous magnetic stirring. The reaction mixture was slightly heated to ~30 °C for 30 min, and then allowed to cool to room temperature. The solution was filtered, and the filtrate was allowed to stand undisturbed for 4 days at ambient temperature, during which time large black needles of **3**·MeOH slowly grew. These were collected by filtration, washed with a little Et_2O, and dried in vacuo; the yield was 75%; the compound can also be crystallized as **3**·MeOH from a $MeOH/Et_2O$ layering. The sample for crystallography was obtained from $MeOH/Et_2O$ and maintained in contact with the mother liquor to prevent degradation of the crystal quality. Vacuum-dried solid analyzed as **3**·$2H_2O$. Anal. Calcd (found) for $C_{101}H_{200}Mn_{12}O_{51}$: C, 41.98 (41.86); H, 6.98 (6.84); N, 0.00 (0.02). Selected IR data (cm^{-1}): 3419 (w), 2954 (vs), 2905 (mw), 2868 (mw), 1572 (vs), 1519 (s), 1412 (vs), 1366 (vs), 1275

(s), 1233 (s), 1198 (s), 1143 (m), 1032 (m), 977 (m), 906 (m), 709 (w), 642 (w), 606 (w), 547 (w), 423 (m).

X-ray Crystallography. Data were collected at 173 K on a Siemens SMART PLATFORM equipped with a CCD area detector and a graphite monochromator utilizing MoK_α radiation ($\lambda = 0.71073$ Å). A suitable crystal of **3**·MeOH was attached to a glass fiber using silicone grease and transferred to the goniostat where it was cooled to −100 °C for characterization and data collection. The structure was solved by the direct methods in *SHELXTL6*, and refined using full-matrix least-squares. The non-H atoms were treated anisotropically, whereas the H atoms were calculated in ideal positions and refined as riding on their respective C atoms. Cell parameters were refined using 8192 reflections. A full sphere of data (1850 frames) was collected using the ω-scan method (0.3° frame width). The first 50 frames were remeasured at the end of data collection to monitor instrument and crystal stability (maximum correction on I was <1%). Absorption corrections by integration were applied based on measured indexed crystal faces.

An initial survey of reciprocal space revealed a set of reflections with a tetragonal lattice. Analysis of the full data set revealed the space group to be $I\bar{4}$. The asymmetric unit consists of one-quarter of the Mn_{12} cluster lying on a $\bar{4}$ axis and one-quarter of a MeOH on another $\bar{4}$ axis. A total of 369 parameters were refined in the final cycle of refinement on F^2 using 7144 reflections with $I > 2\sigma(I)$ to yield R_1 and wR_2 of 3.64 and 10.35%, respectively. Crystal data and structure refinement details are collected in Table 1.

Table 1. Crystal Data and Structure Refinement Parameters for 3·MeOH

parameter	3·MeOH
formula[a]	$C_{101}H_{192}Mn_{12}O_{49}$
fw, g mol^{-1}	2849.83
space group	$I\bar{4}$
a, Å	21.5248(6)
b, Å	21.5248(6)
c, Å	15.2323(8)
V, Å^3	7057.4(5)
Z	2
T, °C	−100(2)
radiation, Å[b]	0.71073
ρ_{calc}, g cm^{-3}	1.341
μ, cm^{-1}	11.08
R1, %[c,d]	3.64
wR2, %[e]	10.35

[a]Including solvent molecules. [b]Graphite monochromator. [c]$I > 2\sigma(I)$. [d]$R_1 = 100\Sigma(||F_o| - |F_c||)/\Sigma|F_o|$. [e]$wR_2 = 100[\Sigma[w(F_o^2 - F_c^2)^2]/\Sigma[w(F_o^2)^2]]^{1/2}$, $w = 1/[\sigma^2(F_o^2) + [(ap)^2 + bp]$, where $p = [\max(F_o^2, O) + 2F_c^2]/3$, and a and b are constants.

DC and AC Magnetometry. Variable-temperature DC magnetic susceptibility data down to 1.80 K were collected at the University of Florida on a Quantum Design MPMS-XL SQUID magnetometer equipped with a 70 kG (7 T) DC magnet. Pascal's constants were used to estimate the diamagnetic corrections, which were subtracted from the experimental susceptibility to give the molar magnetic susceptibility (χ_M). Samples were embedded in solid eicosane, unless otherwise stated, to prevent torquing. Magnetization vs field and temperature data were fit using the program MAGNET.[25] AC magnetic susceptibility data in a 3.5 G field oscillating at frequencies up to 1500 Hz were collected on samples of **3**·MeOH wet with mother liquor or tissue-dried. The latter were prepared by removing crystals from the mother liquor, drying them with tissue paper, and rapidly transferring them to an analytical balance for accurate weight measurement. Then, within 1 min, the crystals were carefully embedded in eicosane within a gelatin capsule in order to ensure no solvent loss or reaction with atmospheric moisture. Ultralow

temperature (<1.8 K) hysteresis studies on single crystals were performed at Grenoble using an array of micro-SQUIDS.[26] The high sensitivity of this magnetometer allows the study of single crystals of SMMs on the order of 10−500 μm, and the field can be applied in any direction by separately driving three orthogonal coils.

High-Frequency Electron Paramagnetic Resonance (HFEPR) Spectroscopy. HFEPR measurements were performed on 3·MeOH at various frequencies in the 50−360 GHz range. Single-crystal spectra were obtained at fixed microwave frequencies and temperatures using a sensitive cavity-perturbation technique, and a Millimeter-wave Vector Network Analyzer (MVNA) was employed as a source and detector (this instrumentation is described in detail elsewhere).[27,28] Angle-dependent measurements were performed in one of two superconducting magnets: a split-pair with a 7 T horizontal field and a vertical access, allowing smooth 180° rotation of the entire EPR probe with <0.1° angle resolution, and a 17 T solenoid for high-field measurements. Both setups allow further rotation of the sample about a horizontal axis by means of a specially designed cylindrical cavity with a rotating end-plate;[28,29] this capability thus enabled true two-axis studies in the 7 T magnet. Very high-frequency easy-axis measurements were performed on higher-order modes of the rotating cavity. Temperature control was achieved within the variable-flow cryostat belonging to a Quantum Design PPMS system.
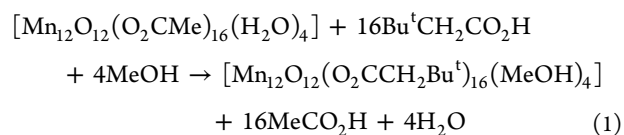
^{55}Mn Nuclear Magnetic Resonance (NMR) Spectroscopy. Crystals of 3·MeOH of suitable dimensions for single-crystal studies were coated in fast-setting epoxy to allow for easier manipulation of the brittle material and to help prevent damage from thermal cycling. NMR coils for the single-crystal sample were made by wrapping Cu wire directly around the encapsulated sample. The single crystal was aligned in the coil such that the c-axis (easy-axis) was perpendicular to the H_1 field produced by the coil. The probe used for zero-field frequency scans was inductively matched and could be tuned over a large range, 200−400 MHz, without having to adjust the matching. Because the breadth of the signal was so large, scans could take anywhere from 3 h to 1 day. Utilizing a stepper motor controlled by the spectrometer to aid in tuning greatly increased the efficiency of this process. The spectrometer, a MagRes 2000, was home-built with quadrature detection. $\pi/2−\pi/2$ pulse sequences were utilized for frequency scanning and spin−lattice relaxation time (T_1) measurements, with pulse times ranging from 500 to 1500 ns. Low temperature T_1 studies were conducted with a Janis ^{3}He system; T_1 was measured over a 0.365−1.5 K range with the coil mounted such that it was in thermal contact with a brass plate touching the thermometer and heater.

Other Studies. Infrared spectra in the 400−4000 cm^{-1} range were recorded in the solid state (KBr pellets) on a Nicolet Nexus 670 FTIR spectrophotometer. Elemental analyses (C, H, N) were performed at the in-house facilities of the University of Florida Chemistry Department.

■ RESULTS AND DISCUSSION

Synthesis. As stated in the Introduction, very efficient methodology is available for substitution of all acetate groups of complex **1** with essentially any other carboxylate, including $Bu^tCO_2^-$. The resulting $[Mn_{12}O_{12}(O_2CCH_2Bu^t)_{16}(H_2O)_4]$ (**2**) does not crystallize in a high symmetry space group, but conversion to $[Mn_{12}O_{12}(O_2CCH_2Bu^t)_{16}(MeOH)_4]$ (**3**) by recrystallization from Et$_2$O/MeOH gave tetragonal ($I\bar{4}$) crystals of 3·MeOH. This inconvenient, two-step procedure from **1** also gives low yields (typically 10−15%). A more convenient (one-step), higher-yield (~75%) preparation from **1** in MeOH was subsequently developed (see Experimental Section), as summarized in eq 1.

$$[Mn_{12}O_{12}(O_2CMe)_{16}(H_2O)_4] + 16Bu^tCH_2CO_2H$$
$$+ 4MeOH \rightarrow [Mn_{12}O_{12}(O_2CCH_2Bu^t)_{16}(MeOH)_4]$$
$$+ 16MeCO_2H + 4H_2O \qquad (1)$$

Description of Structure. A partially labeled ORTEP plot in PovRay format (top) and a stereoview (bottom) of **3** are presented in Figure 1, and a side-view is shown in Figure 2
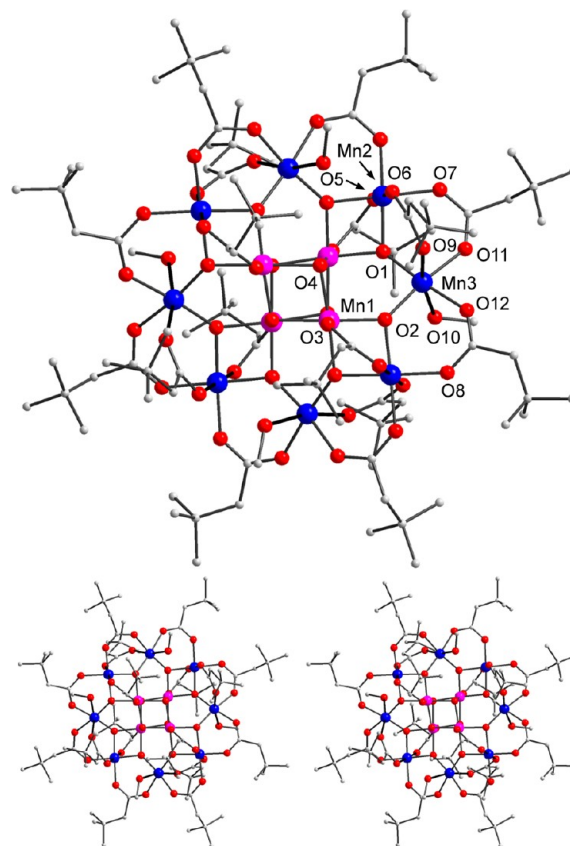

Figure 1. PovRay representations of partially labeled **3** and MeOH solvent molecule (top), and a stereopair (bottom). Color code: Mn^{IV} purple; Mn^{III} blue; O red; C gray.

(top). Selected interatomic distances and angles are listed in Table 2. 3·MeOH crystallizes in the tetragonal space group $I\bar{4}$; the Mn$_{12}$ and MeOH solvent molecules both lie on crystallographic $\bar{4}$ (S_4) axes. For the sake of brevity, references to specific atoms in the following discussion implicitly include their symmetry-related partners. The structure of **3** is typical of a member of this Mn$_{12}$ family, and very similar to that of **1** except for the carboxylate, MeOH vs H$_2$O, and solvent molecule differences. There is a central $[Mn^{IV}_4O_4]^{8+}$ cubane unit (Mn1, O4) held within a nonplanar ring of eight Mn^{III} atoms (Mn2, Mn3) by eight μ_3-O^{2-} ions (O1, O2). Peripheral ligation is provided by 16 η^1:η^1:μ-Bu^{t}CH$_2$CO$_2^-$ and 4 terminal MeOH groups (O10). All the Mn atoms are six-coordinate with near-octahedral geometry. The Mn^{III} atoms exhibit axial Jahn−Teller (JT) elongations by ~0.1−0.2 Å compared with the equatorial bonds, and the JT axes all contain carboxylate and/or MeOH O atoms. They thus avoid the eight μ_3-O^{2-} ions, which is the normal situation in Mn$_{12}$ complexes, and **3** is thus not an example of the rare form of JT isomer in which one or more JT axes are pointed toward a μ_3-O^{2-} ion. The eight JT axes are
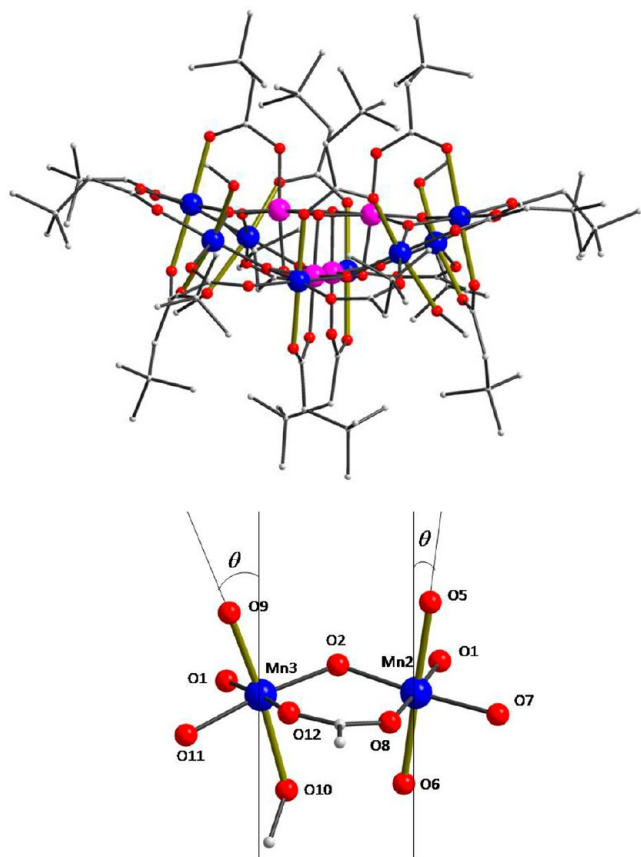
C

dx.doi.org/10.1021/ic301764t | *Inorg. Chem.* XXXX, XXX, XXX−XXX

Figure 2. Side-view of **3** showing the disposition of the JT axes as green bonds (top), and the angle (θ) between the JT axes of Mn2 and Mn3 and the molecular z axis (bottom). Color code: Mn^{IV} purple; Mn^{III} blue; O red; C gray.

Table 2. Selected Core Interatomic Distances (Å) for Complex 3·MeOH[a]

parameter	value
Mn^{IV}–O$_c$ (ax)	1.931(2)
Mn^{IV}–O$_c$ (eq)	1.908(2), 1.907(2)
Mn^{IV}–O$_r$	1.874(1), 1.880(2)
Mn^{IV}–O$_{ax}$	1.913(2)
Mn^{IIIb}–O$_r$	1.895(2), 1.899(2)
Mn^{IIIc}–O$_r$	1.882(2), 1.892(2)
Mn^{IIIb}–O$_{eq}$	1.956(2), 1.932(2)
Mn^{IIIc}–O$_{eq}$	2.118(2), 1.970(2)
Mn^{IIIb}–O$_{ax}$	2.166(2), 2.177(2)
Mn^{IIIc}–O$_{ax}$	2.118(2)
Mn^{IIIc}–O$_M$	2.225(2)
O$_r$–Mn^{IV}–O$_r$	84.97(8)
O$_r$–Mn^{IIIb}–O$_r$	83.84(8)
O$_r$–Mn^{IIIc}–O$_r$	93.62(8)
Mn^{IV}···Mn^{IV}	2.831(1), 2.831(1), 2.928(1)
Mn^{IIIb}···Mn^{IIIc}	3.339(1), 3.425(1)
Mn^{IIIb}···Mn^{IV}···Mn^{IV}	178.36(2), 121.18(2), 122.73(2)
Mn^{IIIb}···Mn^{IV}	2.7720(6)
Mn^{IIIc}···Mn^{IV}	3.456(2), 3.467(1)

[a]O$_c$ = cubane oxide, O$_r$ = ring oxide, O$_{ax}$ = axial carboxylate, O$_{eq}$ = equatorial carboxylate, O$_M$ = methanol. [b]Mn^{III} atom Mn(2). [c]Mn^{III} atom Mn(3).

thus roughly parallel to each other and to the molecular z (S_4) axis, the crystallographic c axis.

The precise orientation (θ) of each JT axis to the z axis will be of relevance to the ^{55}Mn NMR spectral analyses to be described (vide infra), and these data are therefore provided here (Figure 2, bottom). The JT axes at Mn2 and Mn3 are at angles of θ = 13.7° and 36.6°, respectively; for these calculations, each Mn^{III} JT axis was taken as the O···O vector between the two trans Mn–O bonds.

There are no hydrogen-bonding interactions between the Mn$_{12}$ and MeOH solvent molecules. The bulky Bu^{t}CH$_2$ groups prevent close approach of the solvent MeOH groups to the O atoms of bound Bu^{t}CH$_2$CO$_2^-$ or MeOH ligands, and in fact, each solvent MeOH is within a hydrophobic pocket of 12 Bu^t groups from the 4 surrounding Mn$_{12}$ molecules (Figure 3).
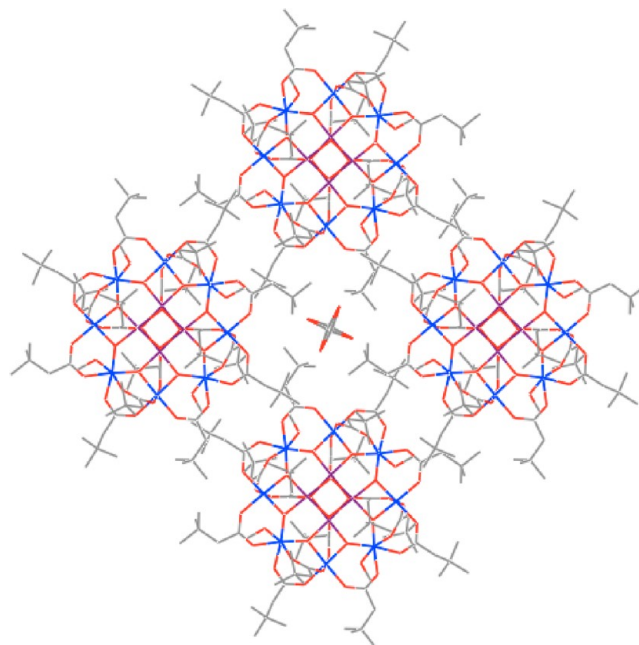

Figure 3. Packing diagram viewed along an S_4 rotation axis (crystallographic c axis) showing the disordered MeOH solvent molecule (center) surrounded by carboxylate Bu^t groups. Color code: Mn^{IV} purple; Mn^{III} blue; O red; C gray.

Thus, unlike the situation in **1**, the solvent molecules in **3·MeOH** cannot provide any hydrogen-bonding contacts to lower the local site-symmetry of the Mn$_{12}$ molecules; i.e., all Mn$_{12}$ molecules retain their crystallographic S_4 (axial) symmetry. The only hydrogen-bonds are intramolecular, between the terminal MeOH ligands and adjacent carboxylate O atoms (O6···O10 = 2.60 Å).

DC Magnetic Susceptibility Studies. Variable-temperature DC magnetic susceptibility (χ_M) data were collected on a powdered, microcrystalline vacuum-dried sample of **3·2H$_2$O**, restrained in eicosane to prevent torquing, in a 1.0 kG magnetic field in the 5.0–300 K range. The resulting $\chi_M T$ vs T plot (Figure S1)[30] is essentially identical with those of previously studied [Mn$_{12}$O$_{12}$(O$_2$CR)$_{16}$(H$_2$O)$_4$] complexes, exhibiting a nearly temperature-independent value of 18–20 cm^3 K mol^{-1} in the 150–300 K range which then increases rapidly to a maximum of 52 cm^3 K mol^{-1} at 10 K before decreasing slightly at lower temperatures. The maximum indicates an S = 10 ground state ($\chi_M T$ = 55 cm^3 K mol^{-1} for g = 2), as expected for a Mn$_{12}$ complex, and the slight decrease at the lowest temperatures primarily due to zero-field splitting (zfs) and

Zeeman effects. The ground state and additional data were obtained from a fit of magnetization (M) data collected in the 1.8−4.0 K range in applied DC fields (H) ranging from 1 to 70 kG. The data are plotted in Figure 4 as reduced magnetization
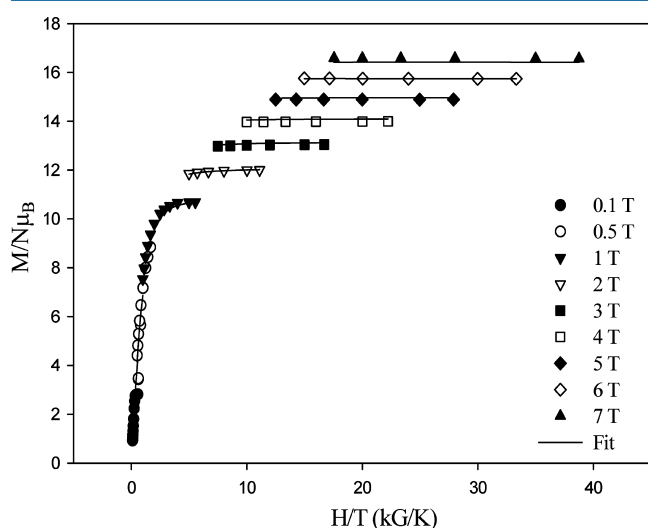

Figure 4. Plot of $M/N\mu_B$ vs H/T for **3**·MeOH at the indicated applied fields. The solid lines are the fit of the data; see text for the fit parameters.

($M/N\mu_B$) vs H/T, where N is Avogadro's number and μ_B is the Bohr magneton. The data were fit using the program MAGNET[25] to a model that assumes only the ground state is populated at these temperatures and magnetic fields, and incorporates an isotropic Zeeman interaction, axial zero-field splitting ($D\hat{S}_z^2$) and a full powder average.[31] The fit (solid lines in Figure 3) gave $S = 10$, $g = 1.90$, and $D = -0.42$ cm^{-1} = -0.60 K, typical values for the Mn$_{12}$ family.

AC Magnetic Susceptibility Studies. Alternating current (AC) magnetic susceptibility data were collected on vacuum-dried, and pristine (wet), microcrystalline samples of **3**·MeOH in the 1.8−10 K range in a 3.5 G AC field, using 25 oscillation frequencies (v) in the 5−1488 Hz range, to probe the magnetization relaxation dynamics. The in-phase (χ'_M, plotted as $\chi'_M T$) and out-of-phase (χ''_M) AC susceptibility signals for representative frequencies are shown in Figure 5. $\chi'_M T$ is ∼54 cm^3 K mol^{-1} above ∼9 K, consistent with $S = 10$ and $g < 2.0$ slightly. At lower temperatures, there is a frequency-dependent decrease in $\chi'_M T$ and a concomitant increase in χ''_M, indicating **3**·MeOH to be an SMM, as expected. There is no second feature in either $\chi'_M T$ or χ''_M, indicating the absence of any faster-relaxing Mn$_{12}$ species in the sample; i.e., it is not a mixture of Jahn−Teller isomers. As mentioned earlier, JT isomerism involves an abnormally oriented Mn^{III} JT axis, which results in smaller barriers to magnetization relaxation and thus a faster-relaxing, so-called lower-temperature (LT) form, whose χ''_M signals are thus at lower temperatures than the normal, higher-temperature (HT), slower-relaxing form.[32,33] The crystal structure showed only normal JT orientations (HT form), but it cannot by itself rule out a small amount of the LT form being present; this is now excluded by the AC data.

The χ''_M vs T plots were used as a source of kinetic data to calculate the effective energy barrier (U_{eff}) to magnetization relaxation.[34] At a given oscillation frequency, v, the χ''_M peak maximum, T_{max}, is the temperature at which the thermal magnetization relaxation rate ($1/\tau = 2\pi v$, where τ is the
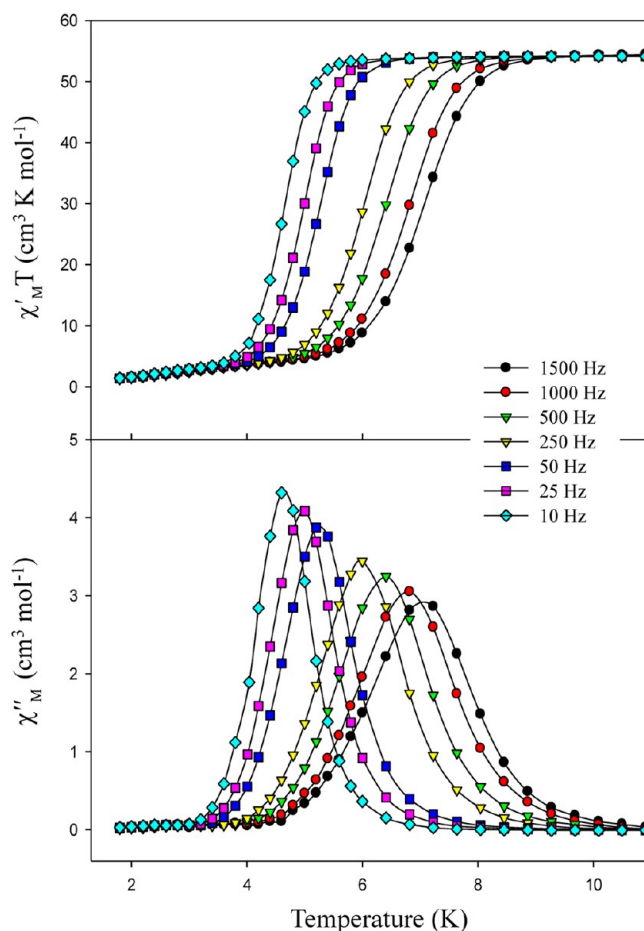

Figure 5. Plot of the in-phase (as $\chi'_M T$) and out-of-phase (χ''_M) AC susceptibility signals vs temperature for dried, microcrystalline complex **3** at the indicated oscillation frequencies.

relaxation time) is just sufficient to keep up with the oscillating driving field. The AC data thus provide relaxation rate vs T data, and these are used to make an Arrhenius plot of log(v) vs $1/T_{max}$ (Figure 6). Each T_{max} value for the χ''_M peaks at the 25
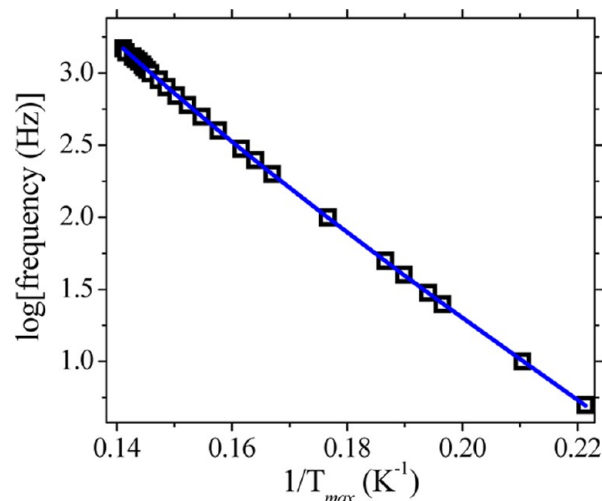

Figure 6. Arrhenius plot of the logarithm of the magnetization relaxation frequency (in Hz) vs $1/T_{max}$ for **3**·MeOH. T_{max} is the temperature of the peak maximum in χ''_M at each oscillation frequency. The solid curve is a fit to eq 2; see the text for the fit parameters.

different oscillation frequencies in the 5–1500 Hz range was accurately determined from a Lorentzian fit to the χ''_M data. As noted in a previous study, the Arrhenius plot is not perfectly linear, indicating the onset of additional relaxation pathways at elevated temperatures; an in-depth discussion of this behavior is available elsewhere,[35] where the double exponential function of eq 2 was employed to fit data such as those in Figure 6.

$$(1/\tau) = (1/\tau_{01}) \exp(-U_1/kT) + (1/\tau_{02}) \exp(-U_2/kT) \tag{2}$$

This empirical formula greatly simplifies the physics associated with the high temperature relaxation processes by simply modeling them as an additional, higher-energy barrier, U_2, with a much faster attempt time, τ_{02}. In spite of this simplification, the formula accurately captures the low temperature limiting behavior, which is dominated by the single barrier, U_1, associated with the $S = 10$ spin multiplet and its associated attempt time, τ_{01}. The fit of the data (solid line in Figure 6) yields the following values: $U_1 = 63(1)$ K, $\tau_{01} = 2.8(6) \times 10^{-8}$ s, $U_2 = 102(4)$ K, and $\tau_{02} = 1.3(7) \times 10^{-10}$ s. Careful comparisons suggest that the obtained U_1 value for **3**·MeOH is slightly higher than for **1** and other derivatives, indicating higher overall crystal purity/symmetry; an in-depth discussion is available elsewhere.[36]

AC in-phase and out-of-phase data vs frequency were collected at a fixed $T = 4.6$ K to allow an Argand (or Cole–Cole plot) to be constructed.[9] A sample of wet crystals was transferred directly into eicosane for these measurements, to prevent all exposure to air. The mass was therefore unknown, and the obtained data are thus the in-phase (m') and out-of-phase (m'') magnetization of the sample. The resulting plot of m' vs m'' for AC frequencies in the 0.1–1488 Hz range is shown in Figure 7. The data were least-squares fit to a single relaxation process (dashed line in Figure 7) and a distribution of single relaxation processes (solid line in Figure 7): the m' (or χ') and m'' (or χ'') as a function of angular frequency (ω) are given by eqs 3 and 4 for a single relaxation process (i.e., a single relaxation barrier, U_{eff}), and by eqs 5 and 6 for a distribution of
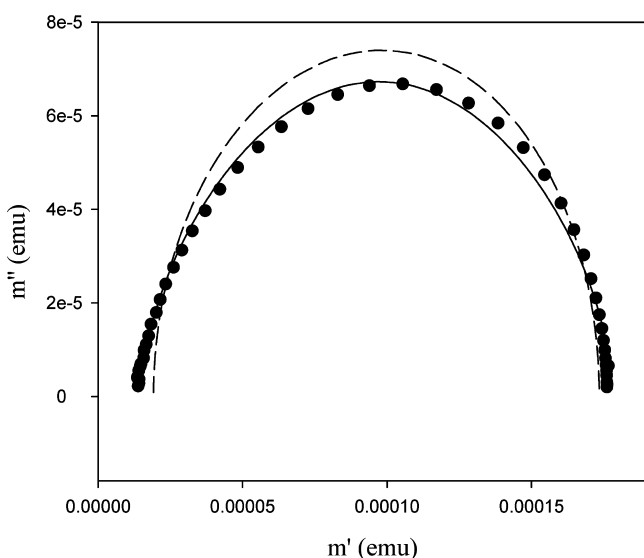
$$\chi'(\omega) = \chi_s + \frac{(\chi_T - \chi_s)}{1 + \omega^2 \tau^2} \tag{3}$$

$$\chi''(\omega) = \frac{(\chi_T - \chi_s)\omega\tau}{1 + \omega^2 \tau^2} \tag{4}$$

$$\chi'(\omega) = \chi_s + \frac{(\chi_T - \chi_s)[1 + (\omega\tau)^{1-\alpha} \sin(\alpha\pi/2)]}{1 + 2(\omega\tau)^{1-\alpha} \sin(\alpha\pi/2) + (\omega\tau)^{2(1-\alpha)}} \tag{5}$$

$$\chi''(\omega) = \frac{(\chi_T - \chi_s)(\omega\tau)^{1-\alpha} \cos(\alpha\pi/2)]}{1 + 2(\omega\tau)^{1-\alpha} \sin(\alpha\pi/2) + (\omega\tau)^{2(1-\alpha)}} \tag{6}$$

single relaxation processes (i.e., a distribution of barriers). In these equations, χ_s is the adiabatic susceptibility, χ_T is the isothermal susceptibility, $\omega = 2\pi\nu$ is the angular frequency, and τ is the relaxation time. A main objective of such a study is assessing the magnitude of α, a value between 0 and 1, included in the expressions for a distribution of relaxation processes; α gauges the width of the distribution. The fit of the data to eqs 3 and 4 (dashed line) is clearly inferior to the fit to eqs 5 and 6 with $\alpha = 0.184$ (solid line). The relaxation times (τ) obtained from the two fits are very similar, $\tau = 0.0176$ s and $\tau = 0.0181$ s, respectively, with the main difference arising from the values of the adiabatic and isothermal susceptibility. We speculate that the distribution of relaxation processes may be caused by weak disorder in the sample, typical of molecular crystals, that facilitates tunneling among states very close to the top of the classical magnetization reversal barrier; i.e., weak disorder gives rise to a small distribution in barrier heights, U_{eff}. It is well documented that disorder can lead to precisely such behavior,[9] and similar α values have been found for other high-symmetry Mn$_{12}$ SMMs.[12] It should be emphasized that such effects should be captured by eqs 5 and 6 because they represent a single relaxation process with a distribution of relaxation times. However, close inspection of the data and fits in Figure 7 reveals a very weak asymmetry in the latter that is not captured by eqs 5 and 6. Such deviations suggest the existence of fundamentally different relaxation processes such as those considered in the analysis of the Arrhenius data (eq 2).

Note that one cannot easily relate α, the distribution in effective barrier U_{eff}, to the distribution in zero-field parameter D measured by EPR (vide infra) that determines the classical barrier U. In the case of a quantum system like an "ideal" Mn$_{12}$, the effective barrier U_{eff} is not fixed; i.e., it will depend on the temperature because for increasing T, higher and higher M_S energy levels are dominating the magnetization reversal. This means that one rarely finds that the U_{eff} barrier is given by D. Consequently, one cannot quantitatively relate the α distribution in barrier height to the D distribution measured by EPR.

Magnetization Hysteresis Loops. Hysteresis in magnetization vs DC field sweeps is the classical property of a magnet. Studies were performed on single crystals of **3**·MeOH using a micro-SQUID apparatus, and the resulting hysteresis loops below 3.6 K at a 0.002 T/s sweep rate, and different sweep rates at 3 K, are shown in Figure 8. The hysteresis loops exhibit increasing coercivity with decreasing temperature and with increasing field sweep rate, as expected for the superparamagnetic properties of a SMM. Hysteresis is observed up to ~3.6 K at a 2 mT/s sweep rate. In addition, as is usually observed for Mn$_{12}$ SMMs, the loops exhibit well-defined steps

Figure 7. Argand plot of m' vs m'' of dried crystals of **3**·2H$_2$O at 4.6 K. The dashed line is a least-squares fit of the data to a single relaxation process given by eqs 3 and 4. The solid line is a fit to a distribution of single relaxation processes given by eqs 5 and 6.
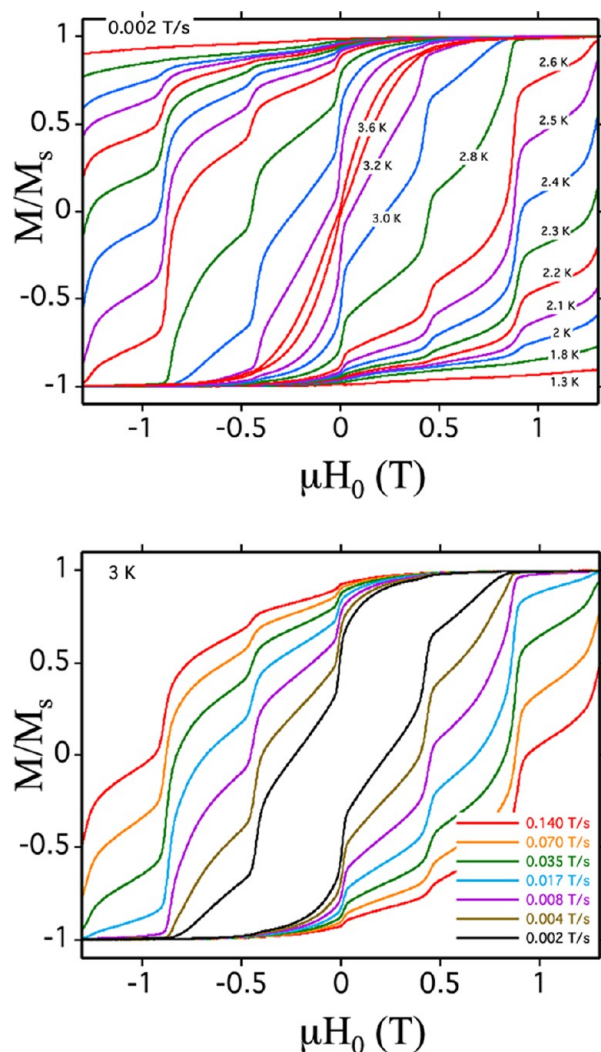
Figure 8. Magnetization hysteresis loops for a single crystal of **3**·MeOH: (top) temperature dependence at a 2 mT/s scan rate; (bottom) scan-rate dependence at 3.0 K. M is normalized to its saturation value, M_s.

due to quantum tunneling of magnetization (QTM) at periodic field values. The latter are those at which m_S levels on one side of the potential energy double well of the $S = 10$ ground state are in resonance with m_S levels on the other side, allowing tunneling to occur through the anisotropy barrier. The steps are thus positions of increased magnetization relaxation rate. The separation between steps, ΔH, is proportional to D, as given in eq 7.

$$\Delta H = \frac{|D|}{g\mu_B} \qquad (7)$$

Measurement of the step positions in Figure 7 gave an average ΔH of 0.45 T and thus a $|D|/g$ value of 0.20 cm^{-1} (0.29 K). Taking g as 2.0, this corresponds to a D value of 0.40 cm^{-1} = 0.58 K, consistent with the values from the magnetization vs field fit on dried samples of **3**·2H$_2$O ($D = -0.42$ cm^{-1}, $g = 1.90$, $|D|/g = 0.22$ cm^{-1}).

High-Frequency EPR (HFEPR) Spectroscopy. In order to determine the effective giant-spin Hamiltonian parameters for **3**·MeOH, and to characterize any disorder in crystals of this compound, we carried out extensive multi-high-frequency EPR

measurements as a function of magnetic field (frequency), field orientation, and temperature. All the EPR data presented below were obtained from carefully oriented single-crystals. The sensitivity of the measurements was enhanced via the use of a unique cavity, which additionally permitted sample rotation relative to the applied field direction.[28] The quality factor of the cavity at its fundamental TE011 mode frequency of 51 GHz is 20 000. However, measurements were also feasible to frequencies well above 300 GHz on high-order modes. The use of a cavity provides additional benefits in terms of being able to control the polarization of the microwave field (H_1) at the position of the sample, and in reducing instrumental problems that can give rise to distorted lineshapes. The use of a network analyzer further enables measurement of both the in-phase (absorption) and out-of-phase (dispersion) response of the sample.[27,28] In order to avoid solvent loss from the samples, the needle shaped single-crystals ($\sim 1 \times 0.4 \times 0.4$ mm) were removed directly from their mother liquor and protected with paratone-N oil before cooling under 1 atm of He gas.

Ignoring nuclear hyperfine interactions, the effective Hamiltonian for an isolated giant-spin molecule with strictly S_4 site symmetry is given to fourth-order in eq 8,[37] with $\hat{O}_4^0$ and $\hat{O}_4^4$ defined as in eqs 9 and 10, respectively. $\hat{S}$ is the spin

$$\hat{H} = D\hat{S}_z^2 + B_4^0\hat{O}_4^0 + B_4^4\hat{O}_4^4 + \mu_B\vec{B}\cdot\vec{g}\cdot\hat{S} \qquad (8)$$

$$\hat{O}_4^0 = 35\hat{S}_z^4 - 30S(S+1)\hat{S}_z^2 + 25\hat{S}_z^2 - 6S(S+1) + 3S^2(S+1)^2 \qquad (9)$$

$$\hat{O}_4^4 = \frac{1}{2}(\hat{S}_x^4 + \hat{S}_y^4) \qquad (10)$$

angular momentum operator and $\hat{S}_i$ the component operators along the i-axis ($i = x, y, z$) of the molecule, $\vec{B}$ is the local magnetic field vector, and $\vec{g}$ is the Landé g-tensor. D parametrizes the dominant axial anisotropy, while B_4^0 and B_4^4 parametrize the fourth-order anisotropy terms $\hat{O}_4^0$ and $\hat{O}_4^4$, respectively. When the applied field is aligned with the S_4 (z-) axis, and assuming $\vec{g}$ is diagonal, the appropriate basis states are defined by the spin projection quantum number m_s, i.e., the projection of the total spin onto the S_4 axis. In this situation, the Hamiltonian matrix is diagonal when written in an $\hat{S}_z$ representation, apart from the transverse $\hat{O}_4^4$ operator, which does not commute with $\hat{S}_z$. However, the effect of this term on the low-lying energy levels is extremely weak for $S = 10$.[29,3f] Consequently, it can be completely neglected as far as the high-frequency EPR (HFEPR) spectrum is concerned, in which case, the energy eigenvalues are given simply by eq 11.

$$E(m_s) \cong D'm_s^2 + Bm_s^4 + g_z\mu_B Bm_s \qquad (11)$$

The relationship between D', B, D and B_4^0 is given elsewhere.[37] Thus, one can directly determine g_z and two of the three zfs parameters in eq 8 by fitting easy-axis EPR spectra to eq 11.

Figure 9 displays 336 GHz easy-axis ($B//z$) HFEPR spectra for complex **3**·MeOH at several temperatures between 1.4 and 30 K. The positions of these peaks are given by the energy differences, $\Delta E = [E(m_s \pm 1) - E(m_s)]$, deduced from eq 11 and given in eq 12, where the + and − denote transitions on

$$\Delta E(m_s) \cong |D'(1 \pm 2m_s) + O(Bm_s^3) \pm g_z\mu_B B| \qquad (12)$$
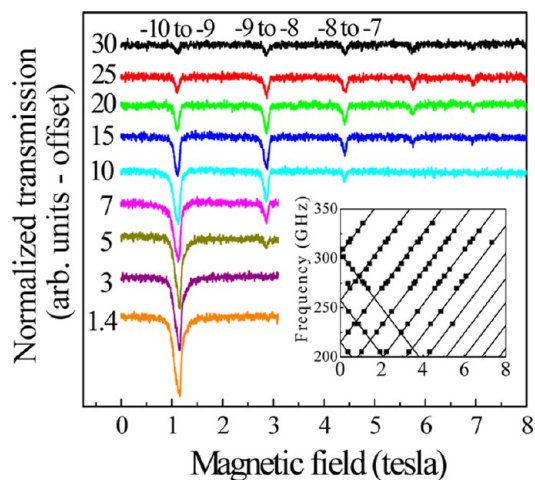
Figure 9. Temperature dependence of the easy-axis HFEPR spectra for **3·MeOH** at a frequency of 336 GHz. The temperatures are in K on the left-hand side of the figure, and several resonances are labeled according to the m_s levels involved in the transition. The inset shows the positions (in field) of resonances deduced from 25 K spectra taken at many frequencies. The solid lines are the fit to eq 12. In order to improve the quality of the fit, a long-range dipolar contribution to the local magnetic induction was included in the analysis.

the negative and positive m_s sides of the barrier, respectively. The approximately linear dependence of the transition energies (frequencies) on m_s results in $2S$ fine- structure features in the HFEPR spectrum, which are more-or-less evenly spaced in magnetic field, as seen in the main panel of Figure 9; several of the resonances have been labeled according to the m_s levels involved in the transition. A slight variation in the spacing between the resonances is due to the fourth-order term in eq 11, which gives rise to a weak term of order Bm_s^3 in eq 12.[7f] By plotting the positions of HFEPR peaks obtained at several different frequencies (inset to Figure 9), one can precisely obtain g_z and the zfs parameters D' and B (hence D and B_4^0) from a fit to an expression similar to eq 12 that includes the full m_s^3 dependence of the transition energies. Such a procedure leads to the following results: $g_z = 1.99(2)$, $D = -0.462(2)$ cm^{-1}, and $B_4^0 = -2.5(2) \times 10^{-5}$ cm^{-1}.[23,24b]

As already discussed, the transverse term, $\hat{O}_4^4$, in eq 8 does not significantly affect the lowest lying zfs for $S = 10$. However, application of a large transverse magnetic field ($B_x > DS/g\mu_B$) results in a situation in which $\hat{O}_4^4$ operates in zeroth-order on the appropriate basis functions; i.e., its contribution to the energy is of order $B_4^4 m_s^4$ in this high-field limit. Furthermore, since it is fourth order in the spin operators, it can contribute to a significant fraction of the anisotropy, i.e., $B_4^4 m_s^4/Dm_s^2 \sim 1\%$. More importantly, the $\hat{O}_4^4$ interaction possesses a very definite symmetry,[37] which is revealed via angle-dependent HFEPR experiments in which the applied field is rotated in the hard plane of the sample.[3f,29,37d,38] Figure 10a shows EPR spectra recorded at 51 GHz for different field orientations within the hard plane of **3·MeOH**. These measurements were restricted to low fields because the higher field transitions are extremely sensitive to small mis-alignments ($<1°$) of the field away from the hard plane.[29] Perfect alignment of the sample within the cavity is not realistic. Therefore, time-consuming two-axis measurements would be required in order to observe the hard-plane dependence of all transitions. However, analysis of the low-field resonances ($\alpha 0$, $\alpha 2$, $\alpha 4$)[29] is sufficient for determining B_4^4. In Figure 10b, a color contour plot of the data in Figure
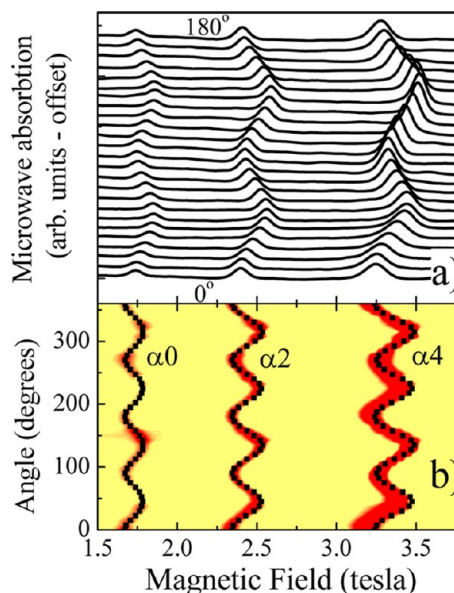

Figure 10. (a) Angle dependence of the hard-plane HFEPR spectra obtained for **3·MeOH** at 15 K and a frequency of 51.5 GHz, for different orientations of the applied field within the hard plane; the angle step is 7.5°, and 0° corresponds to the field parallel to one of the medium axes associated with the fourth-order transverse anisotropy. (b) A color contour plot of the data in (a); the resonances have been labeled according to the scheme in ref 29. The data points represent the best fit to the angle-dependence of the peak positions. From these fits, a unique value for the B_4^4 parameter is obtained.

10a is displayed, albeit spanning the full 360° of rotation. From both plots, a clear oscillatory pattern in the positions of the peaks is observed. The periodicity of the pattern is 4-fold, as expected from the molecular geometry. A good simulation to the peak positions is obtained (solid squares in Figure 10b) using a single value of the parameter $B_4^4 = \pm 4.3(2) \times 10^{-5}$ cm^{-1}, and $g_x = g_y = 1.94(2)$.[23] Detailed studies of simpler (lower nuclearity) SMMs show that sixth and higher order parameters start to become important in the weak-coupling limit.[39] Indeed, in a related study, sixth order parameters were included in the analysis of HFEPR spectra for complex **3·MeOH**.[24c] Given the limited field range explored in the present investigation, it was not possible to further explore this issue, which is anyway beyond the scope of the present paper.

Having explored its zfs parameters, we next assess the quality of crystals of **3·MeOH**. Many groups have demonstrated that the low-temperature quantum dynamics of the most widely studied Mn$_{12}$ complex **1**, are significantly affected by disorder induced by the lattice solvent molecules.[3f,21,23,29,36,37c,d,40] This was first recognized through measurements of so-called D-strain, which indicated a significant distribution of the axial zfs parameter D, with $\sigma_D \approx 0.02D$.[7g,41] Subsequently, it was proposed that this disorder involves hydrogen-bonds between Mn$_{12}$ and acetic acid solvent molecules, as mentioned earlier. This gives rise to a discrete set of Mn$_{12}$ environments and local anisotropies[40b] that lead to differing QTM characteristics.[3f] The main motivation behind the present investigations was to ascertain to what extent crystals of **3·MeOH** might similarly show a range of molecular environments, given that the MeOH molecules are disordered but form no obvious contacts with the Mn$_{12}$ except on the periphery of its bulky Bu^{t}CH$_2$CO$_2^-$ ligand.

The D-strain in **1** was deduced on the basis of a linear m_s dependence of the easy-axis EPR line width.[7g,37c,41] This

dependence can be seen directly from eq 12; i.e., a distribution in D produces an energy broadening that scales linearly with m_s. Figure 11 displays HFEPR line width data for three different S
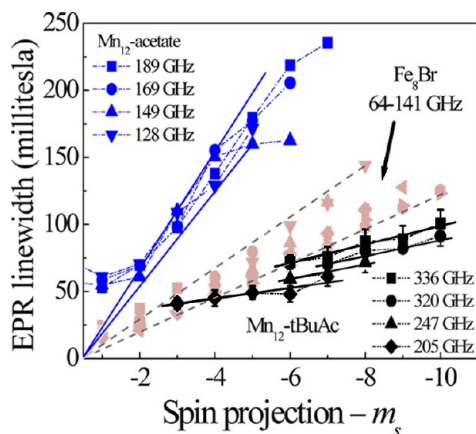

Figure 11. The full-width-at-half-maximum (fwhm) deduced from Gaussian fits to easy-axis HFEPR data obtained for three different $S = 10$ SMMs for a range of frequencies: **1** at 20 K (blue data);[37c] Fe_8Br at 10 K (light gray data);[37c] and Mn_{12}-tBuAc (**3·MeOH**) at 25 K (black data). The horizontal axis denotes the m_s value for the level from which the EPR transition was excited. See main text and eq 12 for explanation of the data.

$= 10$ complexes. For both **1** and Fe_8Br, a significant regime of linear dependence on m_s is observed, with the expected zero-line width intercept at $m_s = -0.5$; the frequency dependence is due to dipolar broadening.[37c,41b] In both **1** and Fe_8Br, the data deviate from a linear dependence for small m_s values, approaching a minimum line width of ~ 50 mT, and is relatively field- (frequency-) independent for **1**. Meanwhile, the minimum line width for Fe_8Br is significantly less and continues to exhibit field dependence. This 'residual' line width results from lesser inhomogeneous broadening mechanisms, which dominate the line width only when the influence of the static D-strain can be minimized (i.e., for transitions involving small m_s values).

The main sources of inhomogeneous broadening, after D-strain, involve local variations (at the molecular level) in the magnetic induction resulting from fluctuating dipolar and nuclear moments. Indeed, the smaller residual line width for Fe_8Br may in part be attributable to the weaker hyperfine coupling in this complex (only ^{57}Fe, $I = 1/2$, 2.1% abundance, has a nuclear spin). The hyperfine contribution to the line width in **1** can be estimated to be on the order of 20 mT,[42] i.e., a good fraction of the observed residual line width. Meanwhile, calculations of the dipolar broadening for transitions involving the lowest $|m_s|$ levels also give linewidths on the order of $10-20$ mT in the $20-25$ K range for **1** (10 mT for Fe_8Br at 10 K). Thus, the residual linewidths for the two previously characterized $S = 10$ systems appear to be caused by a combination of fluctuating nuclear and dipolar fields, together with a residual static D-strain (~ 15 mT for **1**, ~ 6 mT for Fe_8Br). We note that all transitions are sensitive to D strain for an integer spin system.[37a]

The situation concerning the residual line width for **3** should not be so different from **1**, though the dipolar contribution will be somewhat weaker due to the increased Mn_{12} separations. The width for the $m_s = -10$ to -9 transition for **3** is already quite close to the residual line width of **1**, and the linewidths

become comparable at about $m_s = -6$. From the available data for **3**, it appears that the line width levels off for smaller m_s values, approaching an intercept only slightly less than that for **1**, i.e., ~ 35 mT vs ~ 50 mT. Clearly, therefore, the m_s dependence of the line width is much weaker for **3**, implying that the D-strain is considerably weaker than in **1**. Indeed, one can estimate an upper bound of $\sigma_D < 0.0035D$ from the slope of the data for **3·MeOH**, i.e., a factor of $5-6$ less than in **1**. Thus, it is fair to say that the static disorder has been significantly reduced in this new high-symmetry Mn_{12} complex. This and the weaker dipolar broadening thus account for the smaller residual line width (~ 35 mT) for **3·MeOH**.

We believe that the disorder that has been extensively characterized in **1**[3f,29,37d] is unique to that particular complex. In **3·MeOH**, the MeOH solvent molecule is disordered about the S_4 axis, but does not interact strongly with the Mn_{12} core because of the bulky $Bu^tCH_2CO_2^-$ ligands. Among the clearest evidence for the solvent-induced disorder in **1** comes from angle-dependent HFEPR measurements close to the hard plane. Fine structure appears on the high- and low-field sides of the main EPR peaks (Figure 12); each fine-structure feature
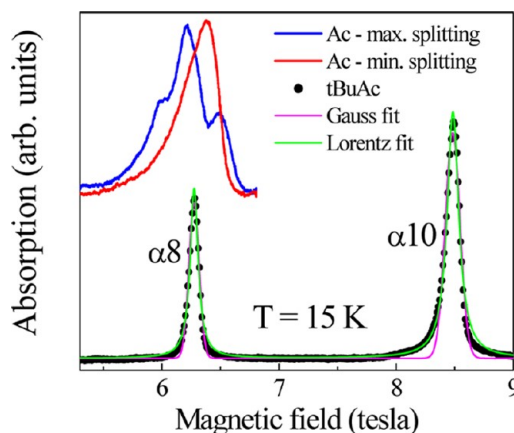

Figure 12. A comparison between the hard-plane HFEPR spectra for **1** and **3·MeOH** at 15 K and 51.5 GHz. Data for **1**, which have been offset for clarity, are only available below 6.8 T. The solvent disorder in **1** gives rise to fine structures (high- and low-field shoulders) that are well resolved from the central peak for some field orientations within the hard plane (blue curve), and unresolved for others (red curve).[37d] These fine structures are completely absent in the data for **3·MeOH**. The thin green and magenta curves are Lorentzian and Gaussian fits to the data, respectively.

corresponds to a distinct Mn_{12} species and exhibits a unique angle-dependence.[3f,29] Such fine-structure features, which are clearly due to the disorder in **1**, are completely absent in the HFEPR spectra of **3·MeOH** (Figure 12). Furthermore, the HFEPR peaks for **3·MeOH** are clearly much sharper than for **1**. These observations constitute the most direct evidence that the type of solvent-induced disorder found in **1** is absent in **3·MeOH**, although this does not rule out other weaker sources of disorder due to, e.g., partial solvent loss, ligand disorder, etc. It is interesting that the hard-plane HFEPR peaks for **3·MeOH** in Figure 12 fit better to a Lorentzian function than to a Gaussian. This could indicate that the line width is limited by the spin dephasing time, implying a T_2 value on the order of 0.3 ns. Future time-resolved HFEPR studies will be needed to resolve this issue.

^{55}Mn NMR Spectroscopy. The obtained NMR spectral and fitting data for **3·MeOH** are collected in Table 3. The

Table 3. ^{55}Mn NMR Peak Parameters for 3·MeOH

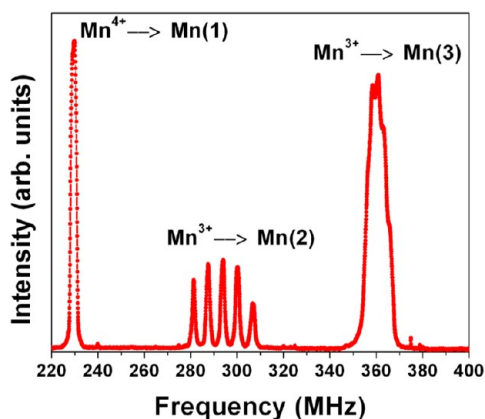| site	electronic spin	central frequency (MHz)	internal field (T)	JT angle with z-axis	$\Delta\nu_Q$ (av) (MHz)	e^2qQ (MHz)
Mn^{4+} Mn(1)	$S = \frac{3}{2}$	229.614	21.868	n/a	0.61	4.06
Mn^{3+} Mn(2)	$S = 2$	293.937	27.994	13.7°	6.35	46.22
Mn^{3+} Mn(3)	$S = 2$	360.833	34.365	36.6°	2.50	35.71

Figure 13. Zero-field ^{55}Mn NMR spectrum of **3·MeOH**. The atom labels Mn(1), Mn(2), and Mn(3) are the same as in Figures 1 and 2.

single-crystal ^{55}Mn NMR spectrum (Figure 13) shows three main peaks, consistent with previously examined Mn$_{12}$ systems.[7c,d,43] The first peak at 229.6 MHz corresponds to the four Mn^{4+} ions in the central cubane, Mn(1). The second peak, centered at 293.9 MHz, belongs to the four outer Mn^{3+} ions, Mn(2), whose local JT axis is at an angle of 13.7° to the molecular z-axis (cell c-axis) (Figure 2 bottom) and is well split by quadrupole couplings. The third peak is centered at 360.8 MHz and is from the other four Mn^{3+} ions, Mn(3), that have their JT axis at an angle of 36.6° to the z-axis. This resonance is also split by quadrupole couplings.

Previous work has defined the hyperfine Hamiltonian that determines the strength of the magnetic field due to interactions of the nuclei with the electrons, and which in turn determines the central frequency of each of the three peaks.[44] The effective hyperfine Hamiltonian is given by eq 13, where H_F is the Fermi contact term, H_d is the dipolar coupling, and H_l is the spin−orbit coupling. It is possible to calculate

$$H_{eff} = H_F + H_d + H_l \tag{13}$$

the Fermi contact and dipolar terms if the magnetic moment at each Mn site has been obtained from neutron studies,[44] but these calculations are not important to this study, and we thus use only the effective hyperfine field.

The Fermi contact term is greatest in magnitude, followed by the dipolar coupling. The spin−orbit coupling term is negligible compared with the other hyperfine interactions and is therefore taken to be zero. The nuclei's energy levels can be further split by nonhyperfine interactions, such as quadrupole (H_Q) or Zeeman (H_0) fields; however, these contributions will be a

small perturbation on the total hyperfine field. The total effective field felt at the nuclear site is then given by eq 14.

$$H_T = H_F + H_d + H_Q + H_0 \tag{14}$$

The Mn^{4+} hyperfine field only has a contribution from the Fermi contact term, while the presence of quadrupolar effects, with respect to spin−lattice relaxation, is still being debated.[45] The Mn^{3+} ions have a combination of the Fermi contact and dipolar fields along with a strong contribution from an electric field gradient, producing quadrupolar interactions. The dominating Fermi contact term produces a range of magnetic fields from 20 to 40 T at the nucleus when considering all three resonances, while the magnitudes of the dipolar hyperfine field and the quadrupole interaction depend on the angle that the local JT axis of the Mn ion makes with the z-axis of the molecule.[44] A larger angle corresponds to a smaller dipolar contribution and a smaller quadrupole coupling. Because the dipolar hyperfine field opposes the Fermi contact term, a smaller dipolar field results in a greater total hyperfine field. This description can clearly be appreciated when comparing the Mn(2) and Mn(3) peaks. Because the Mn(3) peak (360.8 MHz) has a smaller quadrupole splitting and occurs at a higher frequency (larger total hyperfine field), it can be determined that these Mn^{3+} ions are bent away from the z-axis of the molecule by a larger magnitude.

Because of the beautifully resolved quadrupolar peaks, the quadrupole coupling parameter can be extracted using eq 15, assuming the asymmetry parameter, η, is equal to zero. The first

$$E_m = -\gamma_n \hbar H_{eff} m_n + \frac{e^2qQ}{4I(2I-1)}\left(\frac{3\cos^2\theta - 1}{2}\right)$$
$$[3m_n^2 - I(I+1)] \tag{15}$$

term results from the effective hyperfine Hamiltonian while the second term is the quadrupolar perturbation. eQ is the electric quadrupole moment, eq is the gradient of the electric field along the z-axis, and θ is the angle the JT axis makes with the molecular z-axis. Taking the energy difference between two neighboring m_n levels allows the calculation of e^2qQ, the quadrupolar coupling parameter. These values have been reported in a previous publication and are tabulated here.[7d]

Close examination of the Mn(1) resonance shows the presence of 'fingers' at its peak (Figure 14a), an interesting observation considering that, at first glance, the other peaks show no splitting other than quadrupolar, suggesting that quadrupolar forces might not be suppressed at the Mn^{4+} sites. The Mn(1) peak was fit to both Lorentzian and Gaussian line shapes:

$$\text{Gaussian: } y = y_0 + \frac{A}{w\sqrt{\pi/2}}\exp^{-2((x-x_z)/w)^2}$$

$$\text{Lorentzian: } y = y_0 + \left(\frac{2A}{\pi}\right)\left(\frac{w}{4(x-x_c)^2 + w^2}\right)$$

The Gaussian line shape gives the overall best fit (Figure 14a), but neither line function fits perfectly in the wings of the peak. This point will be addressed in more detail after discussion of the line shapes of the Mn(2) and Mn(3) peaks.

The Mn(2) peak was also fit with Lorentzian and Gaussian line shapes (Figure 14b). In this case, the discrepancy between the two functions becomes clear. The Lorentzian line shape closely matches the low frequency wing of the Mn(2) peak,
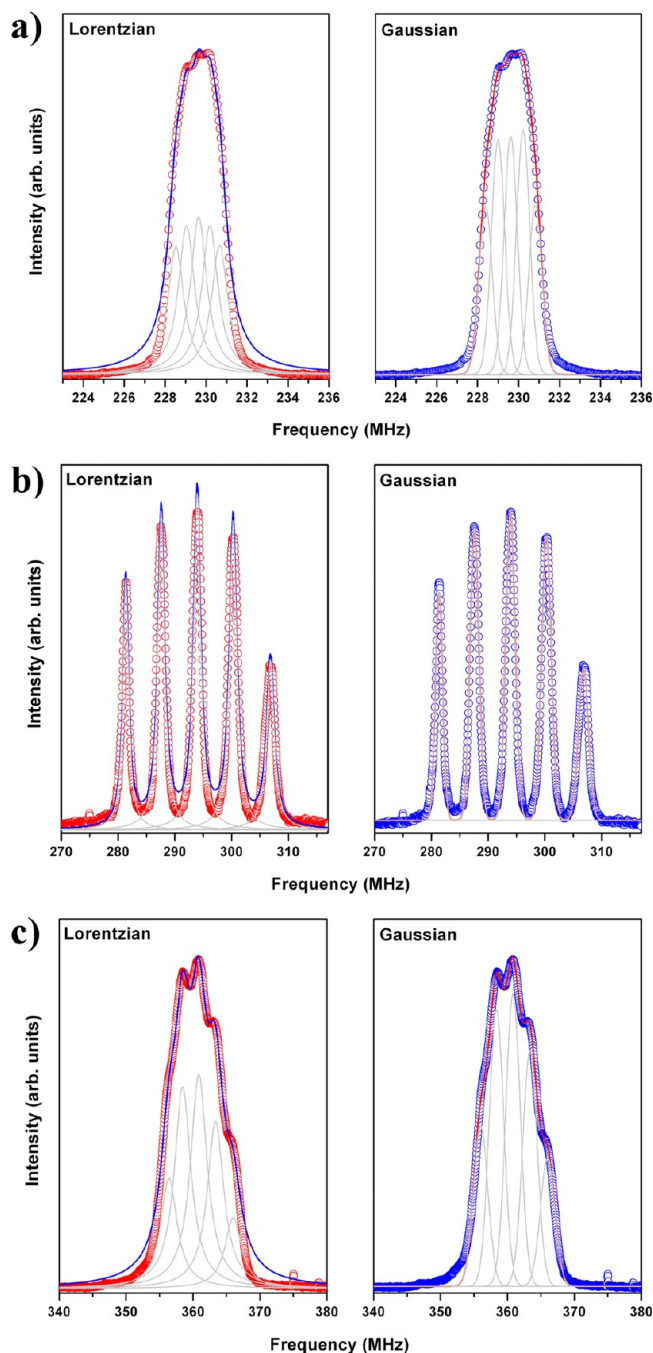
Figure 14. Line fits for the (a) Mn(1), (b) Mn(2) and (c) Mn(3) resonances. The left spectrum is fit to multiple Lorentzian curves while the right spectrum is fit to multiple Gaussian curves. No spectrum fits perfectly well to either line-shape.

while a Gaussian line shape is clearly superior on the high frequency side. To resolve the line shape discrepancy, the area of each of the five resonances was plotted against their width, with both values obtained from the fitting functions (Figure 15, right). Interestingly, the areas of similar transitions are consistent with one another in $3\cdot$MeOH, but the peak width constantly increases. Comparing the line width and peak area of the Mn(2) peak of $3\cdot$MeOH against that of the Mn(2) peak for high symmetry $[Mn_{12}O_{12}(O_2CCH_2Br)_{16}(H_2O)_4]\cdot4CH_2Cl_2$ (Figure 15, left; Mn_{12}−BrAc) emphasizes the inconsistency of the line shapes.

The shift from a Lorentzian to Gaussian line shape obviously is due to the broadening of the resonances upon moving to higher frequencies. One possibility that could explain this behavior would be unusual quadrupole properties, such as a nonzero asymmetry parameter (η), causing the peak locations to be nonsymmetrically distributed about the central transition. Diagonalization of the quadrupolar Hamiltonian was carried out to determine the effect of such an occurrence. Comparing various η values against the peak frequency showed that the shifts present in the Mn(2) peak of $3\cdot$MeOH could not be due to quadrupolar interactions. Looking for consistency, the Mn(3) resonance was then analyzed.

The Mn(3) peak was also fit to Lorentzian and Gaussian line shapes (Figure 14c), and, while there were some similarities to the unusual broadening of the Mn(2) peak, the overlap of the resonances does not allow for a unique set of fitting parameters, making it difficult to determine if in fact broadening occurs as the frequency is increased. Close examination of the line fits for the Mn(3) sites again reveals the presence of a discrepancy at the perimeter of the peak, as the fittings deviate from the baseline. This discrepancy, like that for the Mn(1) peak, may be attributed to the lack of knowledge about the fitting parameters for the peaks that overlap.

Examination of the three main peaks as a whole leads to an inconclusive result. Because at this time it is not possible to attribute the broadening of the Mn(2) resonance to a specific physical interaction, it is difficult to understand, and therefore assign, the origin of the splitting of the Mn(1) peak. More likely than not, the symmetry of the Mn^{4+} ions has decreased allowing the presence of a quadrupole splitting to be observed, presenting the first observable evidence for such an interaction in the Mn^{4+} ions of these Mn_{12} SMMs. The quadrupolar coupling parameter is then calculated in the same manner as it was for the Mn(2) and Mn(3) peaks, with the data included in Table 3. A nonzero quadrupole indicates that Mn_{12}−BrAc is the most symmetric Mn_{12} family member, with respect to the Mn nuclei, as no evidence for splitting is observed for its Mn(1) peak and no broadening is seen in its Mn(2) resonance (Figure 15). The power of single-crystal ^{55}Mn NMR as a technique is obvious with this result, as neither EPR nor X-ray measurements could detail such a fine structure change.

The longitudinal (spin−lattice) relaxation time (T_1) was measured on the Mn(1) peak of $3\cdot$MeOH, as it is the narrowest peak and, therefore, the easiest to saturate. Even though the Mn(1) resonance is the narrowest, it is still difficult to saturate the entire peak, which has a width of 2.8 MHz. Development of a special pulse sequence was necessary and consisted of a comb pulse where the individual pulses occurred at varying frequencies. The set of frequencies was chosen such that the pulses would overlap to blanket the entire peak. Full saturation of the resonance never occurred, but effective saturation was achieved, as the recovery curve could be fit to a single exponential function. The recovery was fit using eq 16, where $M(t)$ is the time-dependent nuclear magnetization, M_∞ is the

$$M(t) = (M_\infty - M_0)[1 - \exp(-t/T_1)] + M_0 \qquad (16)$$

equilibrium magnetization, t is the time between the saturation sequence and the spin−echo observation, and M_0 is the remnant magnetization immediately following the saturation comb. The temperature was then varied and the saturation sequence repeated. T_1 was extracted and plotted as a function of temperature (Figure 16).
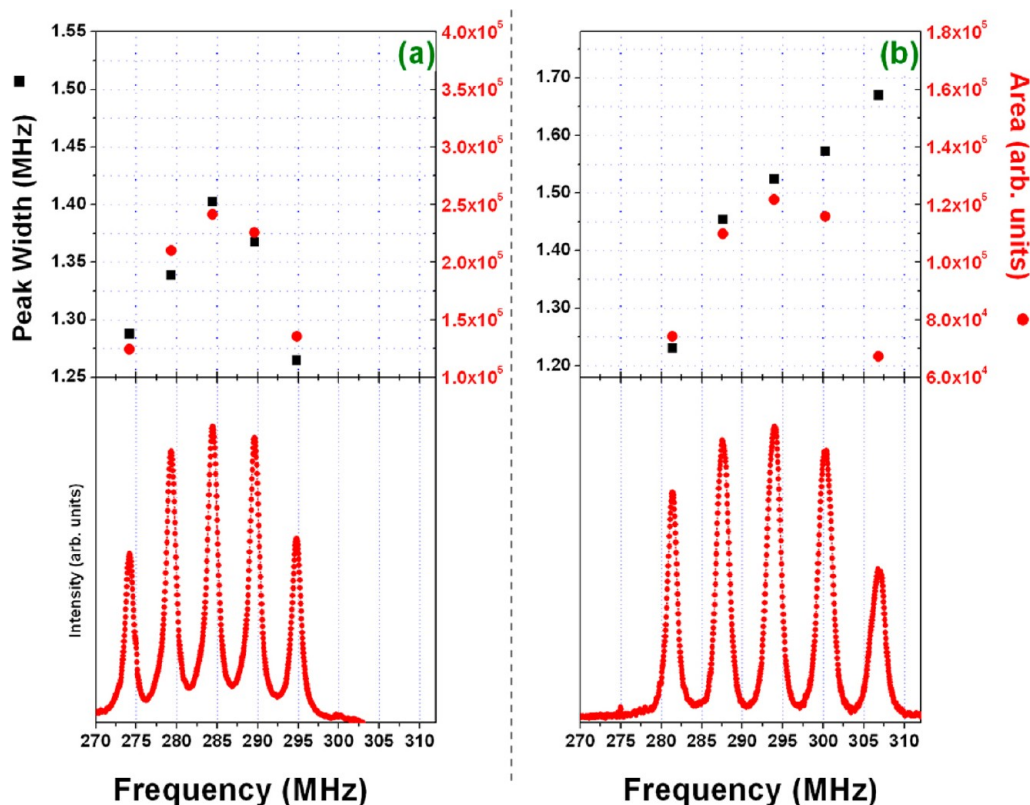
Figure 15. Comparison of the line-width and peak area of the Mn(2) peaks for (a) Mn_{12}–BrAc and (b) **3**·MeOH. The peak width for **3**·MeOH continually increases on moving to higher frequency, an unusual behavior that has yet to be fully explained.
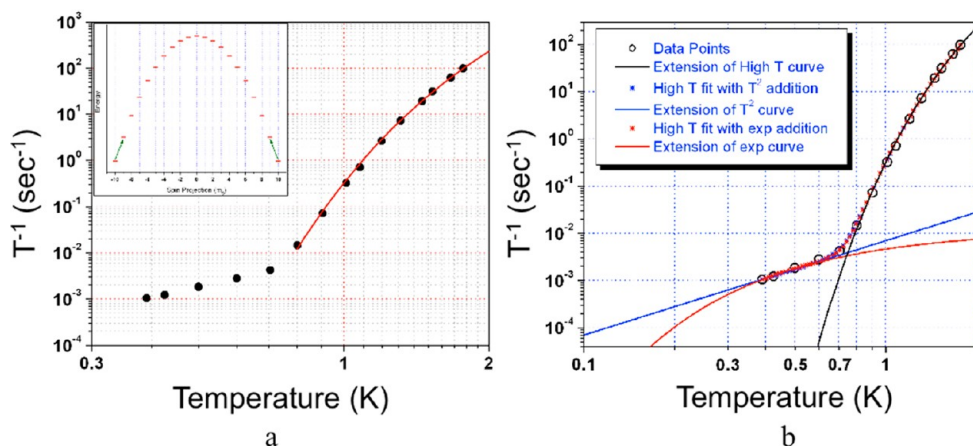

Figure 16. (a) Spin–Lattice relaxation rate (T_1^{-1}) of the Mn(1) peak for a single crystal of **3**·MeOH down to ^{3}He temperatures. Fit of the data gives the activation energy barrier between the $m_S = \pm 10$ and $m_S = \pm 9$ states. (b) T_1^{-1} fits extended down to 100 mK. Dilution-fridge studies are necessary to differentiate the fits.

The high temperature data (0.8–1.8 K) were fit to eq 17 (solid line in Figure 16a), from which the energy barrier

$$\frac{1}{T_1} \propto C \exp(-\Delta E/k_b T) \tag{17a}$$

$$C \propto \frac{\gamma_N^2 \langle h_\perp^2 \rangle}{\omega_N^2 \tau_0} \tag{17b}$$

between the $m_S = \pm 10$ and $m_S = \pm 9$ states was determined to be $\Delta E = 13.1$ K. This is smaller than the $\Delta E = 13.7$ K for Mn_{12}–BrAc. The observed difference is in agreement with that predicted from the D-values from the HFEPR measurements

on the two compounds and provides good support for the essential correctness of the NMR analysis procedure. A slope change occurs at 800 mK, from which a new low-temperature spin–lattice relaxation function evolves. Because it has been previously assumed that T_1 below 0.8 K is temperature-independent, and that tunneling dominates the nuclear relaxation mechanism at these temperatures, no mechanism has been investigated for temperature dependence in this range. To further understand the temperature response, Figure 16b shows the low temperature T_1 data which has been fit with multiple temperature-dependent functions. Equally good fits arise from $T_1^{-1} = \kappa T^2$ and $T_1^{-1} = \kappa \exp(-\Delta E'/k_b T)$, where κ is

L

dx.doi.org/10.1021/ic301764t | *Inorg. Chem.* XXXX, XXX, XXX–XXX

a constant, T is temperature, k_b is the Boltzmann constant, and $\Delta E'$ represents the energy barrier. The physical significance of these fits is currently under investigation.

$\Delta E'$ was extracted from the exponential fit and found to be 1.1 K. While the giant spin model describing this system cannot account for such an energy barrier, it is reminiscent of an initial observation for **1** with another technique, inelastic neutron scattering.[46] This study showed evidence for an energy level that exists roughly 2 K above the ground state, which was found to be magnetic in origin and tentatively associated with the excitation of a dimer, likely between the Mn^{3+} and Mn^{4+} ions. Further neutron experiments on high symmetry Mn_{12} systems could be conducted to determine if in fact any low-lying energy barriers exist.

Another intriguing finding is that ΔE between the $m_S = \pm 10$ and $m_S = \pm 9$ states found by NMR is always less than that observed by EPR or millimeter wave experiments.[3a] In fact, the differences between the values obtained by NMR and EPR are always in the 1–2 K range, when comparing **1**, Mn_{12}–BrAc, and **3·MeOH**. The energy difference is very similar in magnitude to the low-temperature energy barrier, possibly indicating the presence of a much more diverse energy landscape than previously considered, and further rationalizing the need for additional neutron and NMR studies.

To determine which of the low-temperature fits is correct, T_1 measurements must be extended down to 200 mK, a formidable task considering that T_1 is ~1000 s at 400 mK, and, if the fitting trends continue, then T_1 will be anywhere from 5000 to 10 000 s at 200 mK. Such measurements were beyond the scope of the present study, but any future success along these lines could be quite rewarding.

CONCLUSIONS

The synthesis of a new high symmetry Mn_{12} derivative bearing bulky $Bu^tCH_2CO_2^-$ and terminal MeOH ligands has been achieved using a carboxylate substitution reaction in MeOH. The magnetization studies establish that complex **3·MeOH** possesses the usual $S = 10$ ground state spin of the Mn_{12} family, and frequency-dependent out-of-phase AC susceptibility signals and hysteresis loops in magnetization vs applied DC field sweeps confirm it to be an SMM, as expected.

Complex **3·MeOH** thus joins a very small group of Mn_{12} SMMs crystallizing in a tetragonal space group without the mixture of local site-symmetries caused by the hydrogen-bonding contacts with solvent molecules in **1**; in contrast, the lattice MeOH molecule in **3·MeOH** is not hydrogen-bonded to the Mn_{12} core. As a result, the spectra from the sensitive HFEPR and ^{55}NMR spectroscopic techniques are much 'cleaner' than those for **1**, displaying smaller linewidths and superior resolution of fine structure. Comparison of spectra for **3·MeOH** with those for Mn_{12}–BrAc reveals comparable quality, although those for the latter complex are slightly superior in this regard. Nevertheless, **3·MeOH** is much preferred to Mn_{12}–BrAc for detailed study because crystals of the latter lose their CH_2Cl_2 solvent of crystallization extremely rapidly on removal from mother liquor, making it difficult to keep Mn_{12}–BrAc in pristine condition, and leading to broadening of spectroscopic peaks as crystals desolvate. In addition, the bulky CH_2Bu^t groups in **3·MeOH** lead to the magnetic cores of neighboring Mn_{12} molecules being better separated by this insulating hydrocarbon sheaf. Therefore, **3·MeOH** is much closer to the ideal situation of a 3-D

ensemble of identical, monodisperse magnetic particles in identical environments.

The benefits of the above are well displayed in (i) the HFEPR spectra of **3·MeOH**, where the smaller residual line width of the signals suggested significant weakening of the D strain compared to other Mn_{12} complexes; and (ii) the single-crystal ^{55}Mn NMR spectra, where near-baseline resolution of the quadrupole-splitting of one of the Mn^{3+} peaks is observed, and even some faint evidence for quadrupole splitting of the Mn^{4+} peak is noticeable for the first time and assigned to very slight asymmetry around the Mn^{4+} ions. Even though this is not yet thoroughly understood, it could pave the way for more interesting physics, and overall understanding of the relaxation mechanism and QTM processes.

ASSOCIATED CONTENT

Ⓢ Supporting Information

X-ray crystallographic files in CIF format for complex **3·MeOH**. This material is available free of charge via the Internet at http://pubs.acs.org.

AUTHOR INFORMATION

Corresponding Author
*E-mail: christou@chem.ufl.edu. Phone: +1-352-392-8314. Fax: +1-352-392-8757.

Present Addresses
∥Department of Chemistry, University of North Florida, Jacksonville, Florida 32224, United States.
⊥Department of Chemistry, University of Ottawa, Ottawa, Ontario K1N6N5, Canada.

Notes
The authors declare no competing financial interest.

REFERENCES

(1) (a) Christou, G.; Gatteschi, D.; Hendrickson, D. N.; Sessoli, R. *MRS Bull.* **2000**, *25*, 66. (b) Aromi, G.; Brechin, E. K. *Struct. Bonding (Berlin)* **2006**, *122*, 1. (c) Christou, G. *Polyhedron* **2005**, *24*, 2065.

(2) (a) Sessoli, R.; Tsai, H. L.; Schake, A. R.; Wang, S.; Vincent, J. B.; Folting, K.; Gatteschi, D.; Christou, G.; Hendrickson, D. N. *J. Am. Chem. Soc.* **1993**, *115*, 1804. (b) Sessoli, R.; Gatteschi, D.; Caneschi, A.; Novak, M. A. *Nature* **1993**, *365*, 141.

(3) (a) Morello, A.; Bakharev, O. N.; Brom, H. B.; de Jongh, L. J. *Polyhedron* **2003**, *22*, 1745. (b) Caneschi, A.; Ohm, T.; Paulsen, C.; Rovai, D.; Sangregorio, C.; Sessoli, R. *J. Magn. Magn. Mater.* **1998**, *177–181*, 1330. (c) Brechin, E. K.; Boskovic, C.; Wernsdorfer, W.; Yoo, J.; Yamaguchi, A.; Sanudo, E. C.; Concolino, T. R.; Rheingold, A. L.; Ishimoto, H.; Hendrickson, D. N.; Christou, G. *J. Am. Chem. Soc.* **2002**, *124*, 9710. (d) Gatteschi, D.; Sessoli, R. *Angew. Chem., Int. Ed.* **2003**, *42*, 268. (e) Ruiz, D.; Sun, Z.; Albela, B.; Folting, K.; Ribas, J.; Christou, G.; Hendrickson, D. N. *Angew. Chem., Int. Ed.* **1998**, *37*, 300. (f) del Barco, E.; Kent, A. D.; Hill, S.; North, J. M.; Dalal, N. S.; Rumberger, E. M.; Hendrickson, D. N.; Chakov, N.; Christou, G. *J. Low Temp. Phys.* **2005**, *140*, 119. (g) Stamp, P. C. E. *Nature* **1996**, *383*, 125.

(4) Wernsdorfer, W.; Bhaduri, S.; Boskovic, C.; Christou, G.; Hendrickson, D. N. *Phys. Rev. B* **2002**, *65*, 180403(1–4).

(5) (a) Wernsdorfer, W.; Chakov, N. E.; Christou, G. *Phys. Rev. Lett.* **2005**, *95*, 037203/1. (b) Wernsdorfer, W.; Sessoli, R. *Science* **1999**,

284, 133. (c) Wernsdorfer, W.; Soler, M.; Christou, G.; Hendrickson, D. N. *J. Appl. Phys.* **2002**, *91*, 7164.

(6) (a) Jaafar, R.; McHugh, S.; Suzuki, Y.; Sarachik, M. P.; Myasoedov, Y.; Zeldov, E.; Shtrikman, H.; Bagai, R.; Christou, G. *J. Magn. Magn. Mater.* **2008**, *320*, 695−698. (b) McHugh, S.; Jaafar, R.; Sarachik, M. P.; Myasoedov, Y.; Finkler, A.; Shtrikman, H.; Zeldov, E.; Bagai, R.; Christou, G. *Phys. Rev. B* **2007**, *76*, 172410. (c) Suzuki, Y.; Sarachik, M. P.; Chudnovsky, E. M.; McHugh, S.; Gonzalez-Rubio, R.; Avraham, N.; Myasoedov, Y.; Zeldov, E.; Shtrikman, H.; Chakov, N. E.; Christou, G. *Phys. Rev. Lett.* **2005**, *95*, 147201. (d) Macià, F.; Hernandez, J. M.; Tejada, J.; Datta, S.; Hill, S.; Lampropoulos, C.; Christou, G. *Phys. Rev. B* **2009**, *79*, 092403.

(7) (a) Hill, S.; Edwards, R. S.; Aliaga-Alcalde, N.; Christou, G. *Science* **2003**, *302*, 1015. (b) Macia, F.; Lawrence, J.; Hill, S.; Hernandez, J. M.; Tejada, J.; Santos, P. V.; Lampropoulos, C.; Christou, G. *Phys. Rev. B* **2008**, *77*, 020403. (c) Harter, A. G.; Chakov, N. E.; Achey, R.; Reyes, A.; Kuhns, P.; Christou, G.; Dalal, N. S. *Polyhedron* **2005**, *24*, 2346. (d) Harter, A. G.; Lampropoulos, C.; Murugesu, M.; Kuhns, P.; Reyes, A.; Christou, G.; Dalal, N. S. *Polyhedron* **2007**, 2320. (e) Petukhov, K.; Hill, S.; Chakov, N. E.; Abboud, K. A.; Christou, G. *Phys. Rev. B* **2004**, *70*, 054426. (f) Perenboom, J.; Brooks, J. S.; Hill, S.; Hathaway, T.; Dalal, N. S. *Phys. Rev. B* **1998**, *58*, 330. (g) Park, K.; Novotny, M. A.; Dalal, N. S.; Hill, S.; Rikvold, P. A. *Phys. Rev. B* **2002**, *65*, 014426.

(8) (a) Bogani, L.; Wernsdorfer, W. *Nature Mat.* **2008**, *7*, 179. (b) Leuenberger, M. N.; Loss, D. *Nature* **2001**, *410*, 789. (c) Tejada, J.; Chudnovsky, E. M.; del Barco, E.; Hernandez, J. M.; Spiller, T. P. *Nanotechnology* **2001**, *12*, 181.

(9) Bagai, R.; Christou, G. *Chem. Soc. Rev.* **2009**, *38*, 1011 and references therein..

(10) Lis, T. *Acta Crystallogr., Sect. B: Struct. Sci.* **1980**, *36*, 2042.

(11) (a) Eppley, H. J.; Tsai, H.-L.; de Vries, N.; Folting, K.; Christou, G.; Hendrickson, D. N. *J. Am. Chem. Soc.* **1995**, *117*, 301. (b) Kuroda-Sowa, T.; Nakano, M.; Christou, G.; Hendrickson, D. N. *Polyhedron* **2001**, *20*, 1529. (c) Soler, M.; Artus, P.; Folting, K.; Huffman, J. C.; Hendrickson, D. N.; Christou, G. *Inorg. Chem.* **2001**, *40*, 4902. (d) Eppley, H. J.; Christou, G. *Inorg. Synth.* **2002**, *33*, 61.

(12) Chakov, N. E.; Lawrence, J.; Harter, A. G.; Hill, S. O.; Dalal, N. S.; Wernsdorfer, W.; Abboud, K. A.; Christou, G. *J. Am. Chem. Soc.* **2006**, *128*, 6975.

(13) Chakov, N. E.; Zakharov, L. N.; Rheingold, A. L.; Abboud, K. A.; Christou, G. *Inorg. Chem.* **2005**, *44*, 4555.

(14) (a) Soler, M.; Artus, P.; Folting, K.; Huffman, J. C.; Hendrickson, D. N.; Christou, G. *Inorg. Chem.* **2001**, *40*, 4902. (b) Pacchioni, M.; Cornia, A.; Fabretti, A. C.; Zobbi, L.; Bonacchi, D.; Caneschi, A.; Chastanet, G.; Gatteschi, D.; Sessoli, R. *Chem. Commun.* **2004**, 2604.

(15) (a) Artus, P.; Boskovic, C.; Yoo, Y.; Streib, W. E.; Brunel, L.-C.; Hendrickson, D. N.; Christou, G. *Inorg. Chem.* **2001**, *40*, 4199. (b) Boskovic, C.; Pink, M.; Huffman, J. C.; Hendrickson, D. N.; Christou, G. *J. Am. Chem. Soc.* **2001**, *123*, 9914. (c) Kuroda-Sowa, T.; Fukuda, S.; Miyoshi, S.; Maekawa, M.; Munakata, M.; Miyasaka, H.; Yamashita, M. *Chem. Lett.* **2002**, 682. (d) Chakov, N. E.; Wernsdorfer, W.; Abboud, K. A.; Hendrickson, D. N.; Christou, G. *Dalton Trans.* **2003**, 2243. (e) Kuroda-Sowa, T.; Handa, T.; Kotera, T.; Maekawa, M.; Munakata, M.; Miyasaka, H.; Yamashita, M. *Chem. Lett.* **2004**, *33*, 540. (f) Bian, G. Q.; Kuroda-Sowa, T.; Konaka, H.; Hatano, M.; Maekawa, M.; Munakata, M.; Miyasaka, H.; Yamashita, M. *Inorg. Chem.* **2004**, *43*, 4790.

(16) (a) Tsai, H.-L.; Hendrickson, D. N.; Eppley, H. J.; de Vries, N.; Folting, K.; Christou, G. *J. Chem. Soc., Chem. Commun.* **1994**, 1745. (b) Chakov, N. E.; Soler, M.; Wernsdorfer, W.; Abboud, K. A.; Christou, G. *Inorg. Chem.* **2005**, *44*, 5304.

(17) (a) Soler, M.; Chandra, S. K.; Ruiz, D.; Huffman, J. C.; Hendrickson, D. N.; Christou, G. *Polyhedron* **2001**, *20*, 1279. (b) Soler, M.; Wernsdorfer, W.; Abboud, K. A.; Huffman, J. C.; Davidson, E. R.; Hendrickson, D. N.; Christou, G. *J. Am. Chem. Soc.* **2003**, *135*, 3576. (c) Soler, M.; Wernsdorfer, W.; Abboud, K. A.; Hendrickson, D. N.; Christou, G. *Polyhedron* **2003**, *22*, 1777.

(18) Bagai, R.; Christou, G. *Inorg Chem* **2007**, *46*, 10810.

(19) Bian, G.-Q.; Kuroda-Sowa, T.; Gunjima, N.; Maekawa, M.; Munakata, M. *Inorg. Chem. Commun.* **2005**, *8*, 208.

(20) Lampropoulos, C.; Redler, G.; Data, S.; Abboud, K. A.; Hill, S.; Christou, G. *Inorg. Chem.* **2010**, *49*, 1325.

(21) Cornia, A.; Sessoli, R.; Sorace, L.; Gatteschi, D.; Barra, A. L.; Daiguebonne, C. *Phys. Rev. Lett.* **2002**, *89*, 257201.

(22) (a) Tsai, H.-L.; Chen, D.-M.; Yang, C.-I.; Jwo, T.-Y.; Wur, C.-S.; Lee, G.-H.; Wang, Y. *Inorg. Chem. Commun.* **2001**, *4*, 511. (b) An, J.; Chen, Z.-D.; Zhang, X.-X.; Raubenheimer, H. G.; Esterhuysen, C.; Gao, S.; Xu, G.-X. *Dalton Trans.* **2001**, *22*, 3352.

(23) Hill, S.; Anderson, N.; Wilson, A.; Takahashi, S.; Petukhov, K.; Chakov, N. E.; Murugesu, M.; North, J. M.; del Barco, E.; Kent, A. D.; Dalal, N. S.; Christou, G. *Polyhedron* **2005**, *24*, 2284.

(24) (a) Achey, R.; Reyes, A.; Kuhns, P.; Christou, G.; Dalal, N. S. *Inorg. Chem.* **2005**, *44*, 2122. (b) Hill, S.; Anderson, N.; Wilson, A.; Takahashi, S.; Chakov, N. E.; Murugesu, M.; North, J. M.; Dalal, N. S.; Christou, G. *J. Appl. Phys.* **2005**, *97*, 10M510. (c) Barra, A.-L.; Caneschi, A.; Cornia, A.; Gatteschi, D.; Gorini, L.; Heiniger, L.-P.; Sessoli, R.; Sorace, L. *J. Am. Chem. Soc.* **2007**, *129*, 10754. (d) Wernsdorfer, W.; Murugesu, M.; Tasiopoulos, A. J.; Christou, G. *Phys. Rev. B* **2005**, *72*, 212406. (e) Wernsdorfer, W.; Murugesu, M.; Christou, G. *Phys. Rev. Lett.* **2006**, *96*, 057208.

(25) Davidson, E. R. *MAGNET*; Indiana University: Bloomington, IN, 1999.

(26) Wernsdorfer, W. *Adv. Chem. Phys.* **2001**, *118*, 99.

(27) Mola, M; Hill, S.; Goy, P.; Gross, M. *Rev. Sci. Instrum.* **2000**, *71*, 186.

(28) Takahashi, S.; Hill, S. *Rev. Sci. Instrum.* **2005**, *76*, 023114.

(29) Takahashi, S.; Edwards, R. S.; North, J. M.; Hill, S.; Dalal, N. S. *Phys. Rev. B* **2004**, *70*, 094429.

(30) See Supporting Information.

(31) Aliaga-Alcalde, N.; Edwards, R. S.; Hill, S. O.; Wernsdorfer, W.; Folting, K.; Christou, G. *J. Am. Chem. Soc.* **2004**, *126*, 12503.

(32) (a) Sun, Z.; Ruiz, D.; Dilley, N. R.; Soler, M.; Ribas, J.; Folting, K.; Maple, M. B.; Christou, G.; Hendrickson, D. N. *Chem. Commun.* **1999**, *19*, 1973. (b) Aubin, S. M. J.; Sun, Z.; Eppley, H. J.; Rumberger, E. M.; Guzei, I. A.; Folting, P. K.; Gantzel, P. K.; Rheingold, A. L.; Christou, G.; Hendrickson, D. N. *Polyhedron* **2001**, *20*, 1139. (c) Hill, S.; Murugesu, M.; Christou, G. *Phys. Rev. B* **2009**, *80*, 174416.

(33) Soler, M.; Wernsdorfer, W.; Sun, Z.; Huffman, J. C.; Hendrickson, D. N.; Christou, G. *Chem. Commun.* **2003**, *21*, 2672.

(34) Novak, M. A.; Sessoli, R. In *Quantum Tunneling of Magnetization − QTM '94*; Gunther, L., Barbara, B., Eds.; Kluwer: Amsterdam, 1995; pp 171−188.

(35) Lampropoulos, C.; Hill, S.; Christou, G. *ChemPhysChem* **2009**, *10*, 2397.

(36) Redler, G.; Lampropoulos, C.; Datta, S.; Koo, C.; Stamatatos, T. C.; Chakov, N. E.; Christou, G.; Hill, S. *Phys. Rev. B* **2009**, *80*, 094408.

(37) (a) Barra, A. L.; Gatteschi, D.; Sessoli, R. *Phys. Rev. B* **1997**, *56*, 8192. (b) Hill, S.; Perenboom, J. A. A.; Dalal, N. S.; Hathaway, T.; Stalcup, T.; Brooks, J. S. *Phys. Rev. Lett.* **1998**, *80*, 2453. (c) Hill, S.; Maccagnano, S.; Park, K.; Achey, R. M.; North, J. M.; Dalal, N. S. *Phys. Rev. B* **2002**, *65*, 224410. (d) Hill, S.; Edwards, R. S.; Jones, S. I.; North, J. M.; Dalal, N. S. *Phys. Rev. Lett.* **2003**, *90*, 217204.

(38) Kirman, C.; Lawrence, J.; Hill, S.; Yang, E.-C.; Hendrickson, D. N. *J. Appl. Phys.* **2005**, *97*, 10M501.

(39) (a) Wilson, A.; Lawrence, J.; Yang, E.-C.; Nakano, M.; Hendrickson, D. N.; Hill, S. *Phys. Rev. B* **2006**, *74*, R140403. (b) Lawrence, J.; Hill, S.; Yang, E.-C.; Hendrickson, D. N. *Phys. Chem. Chem. Phys.* **2009**, *11*, 6743. (c) Hill, S.; Datta, S.; Liu, J.; Inglis, R.; Milios, C. J.; Feng, P. L.; Henderson, J. J.; del Barco, E.; Brechin, E. K.; Hendrickson, D. N. *Dalton Trans.* **2010**, *39*, 4693. (d) Liu, J.; del Barco, E.; Hill, S. *Phys. Rev. B* **2012**, *85*, 014206.

(40) (a) Chudnovsky, E. M.; Garanin, D. A. *Phys. Rev. Lett.* **2001**, *87*, 187203. (b) del Barco, E.; Kent, A. D.; Rumberger, E. M.; Hendrickson, D. N.; Christou, G. *Europhys. Lett.* **2002**, *60*, 768. (c) del Barco, E.; Kent, A. D.; Rumberger, E. M.; Hendrickson, D. N.; Christou, G. *Phys. Rev. Lett.* **2003**, *91*, 047203. (d) Mertes, K. M.;

Suzuki, Y.; Sarachik, M. P.; Paltiel, Y.; Shtrikman, H.; Zeldov, E.; Rumberger, E.; Hendrickson, D. N.; Christou, G. *Phys. Rev. Lett.* **2001**, *87*, 227205. (e) Bircher, R.; Chaboussant, G.; Sieber, A.; Güdel, H. U.; Mutka, H. *Phys. Rev. B* **2004**, *70*, 212413.

(41) (a) Parks, B.; Loomis, J.; Rumberger, E.; Hendrickson, D. N.; Christou, G. *Phys. Rev. B* **2001**, *64*, 184426. (b) Park, K.; Novotny, M. A.; Dalal, N. S.; Hill, S.; Rikvold, P. A. *Phys. Rev. B* **2002**, *66*, 144409.

(42) Wernsdorfer, W.; Sessoli, R.; Gatteschi, D. *Europhys. Lett.* **1999**, *47*, 254.

(43) Goto, T.; Kubo, T.; Koshiba, T.; Fujii, Y.; Oyamada, A.; Arai, J.; Takeda, K.; Awaga, K. *Physica B* **2000**, *284–288*, 1227.

(44) Kubo, T.; Goto, T.; Koshiba, T.; Takeda, K.; Awaga, K. *Phys. Rev. B* **2002**, *65*, 224425.

(45) Morello, A.; de Jongh, L. J. *Phys. Rev. B* **2007**, *76*, 184425.

(46) Hennion, M.; Pardi, L.; Mirebeau, I.; Suard, E.; Sessoli, R.; Caneschi, A. *Phys. Rev. B* **1997**, *56*, 8819.